Engineering and Technology
2015; 2(4): 235-255
Published online June 30, 2015 (http://www.aascit.org/journal/et)

American Association for Science and Technology

Keywords
Sparlat and Allmaras Model, Jacon and Knight Model, Menter and Rumsey Model, Gibson and Dafa'Alla Model, Reynolds Averaged Navier-Stokes Equations, Algebraic and Two-Equation Turbulence Models

Received: June 7, 2015
Revised: June 13, 2015
Accepted: June 14, 2015

Assessment of Several Turbulence Models as Applied to Supersonic Flows in 2D – Part III

Edisson S. G. Maciel

Aeronautical Engineering Division (IEA), ITA (Aeronautical Technological Institute), SP, Brazil

Email address
edisavio@edissonsavio.eng.br

Citation
Edisson S. G. Maciel. Assessment of Several Turbulence Models as Applied to Supersonic Flows in 2D – Part III. *Engineering and Technology.* Vol. 2, No. 4, 2015, pp. 235-255.

Abstract
In the present work, the Van Leer flux vector splitting scheme is implemented to solve the two-dimensional Favre-averaged Navier-Stokes equations. The Sparlat and Allmaras one-equation model and the Jacon and Knight, Menter and Rumsey, and Gibson and Dafa'Alla two-equation models are used in order to close the problem. The physical problem under study is the supersonic flow around a simplified version of the VLS (Brazilian "Satellite Launcher Vehice") configuration. The results have demonstrated that the stagnation pressure ahead of the VLS configuration is better predicted by the Menter and Rumsey turbulence model in its BSL variant.

1. Introduction

Conventional non-upwind algorithms have been used extensively to solve a wide variety of problems ([1]). Conventional algorithms are somewhat unreliable in the sense that for every different problem (and sometimes, every different case in the same class of problems) artificial dissipation terms must be specially tuned and judicially chosen for convergence. Also, complex problems with shocks and steep compression and expansion gradients may defy solution altogether.

Upwind schemes are in general more robust but are also more involved in their derivation and application. Some upwind schemes that have been applied to the Euler equations are: [2-3]. Some comments about these methods are reported in [4]. The interested reader is encouraged to read this reference to become aware of the present study.

In relation to turbulent flow simulations, [5] applied the Navier-Stokes equations to transonic flows problems along a convergent-divergent nozzle and around the NACA 0012 airfoil. The [6] model was used to close the problem. Three algorithms were implemented: the [7] explicit scheme, the [8] implicit scheme and the [9] explicit scheme. The results have shown that, in general terms, the [7] and the [9] schemes have presented better solutions.

[10] have performed a study involving three different turbulence models. In this work, the Navier-Stokes equations were solved applied to the supersonic flow around a simplified configuration of the Brazilian Satellite Launcher, VLS. The algebraic models of [11] and of [6] and the one-equation model of [12] were used to close the problem. The algorithms of [13] and of [3] were compared and presented good results.

In terms of two-equation models, [14] have presented a work that deals with such models applied to the solution of supersonic aerospace flow problems. The two-dimensional Navier-Stokes equations written in conservative form, employing a finite volume formulation and a structured spatial discretization were solved. The [2] algorithm, first order accurate in space, was used to perform the numerical experiments.

Turbulence was taken into account using two k-ε turbulence models, namely: the [15-16] models. The steady state supersonic flow around a simplified version of the Brazilian Satellite Launcher, VLS, configuration was studied. The results have shown that the pressure field generated by the [16] model was stronger than the respective one obtained with the [15] model, although the latter predicts more accurate aerodynamic coefficients in this problem. The [16] model predicted less intense turbulence kinetic energy- and dissipation-rate profiles than the [15] model, yielding less intense turbulence fields.

In the present work, the [2] flux vector splitting scheme is implemented, on a finite-volume context. The two-dimensional Favre-averaged Navier-Stokes equations are solved using an upwind discretization on a structured mesh. The [17] one-equation model and the [18-20] two-equation models are used in order to close the problem. The physical problem under study is the supersonic flow around a simplified version of the VLS configuration. The implemented scheme uses a MUSCL procedure to reach second order accuracy in space. The time integration uses a Runge-Kutta method of five stages and is second order accurate. The algorithm is accelerated to the steady state solution using a spatially variable time step. This technique has proved excellent gains as reported in [21-22].

The results have demonstrated that the [19] model has yielded more critical temperature fields than the other models. The aerodynamic coefficient of lift is better predicted by the [20] turbulence model in its Chien-Launder and Sharma variant, with the [19] in its BSL variant in second place. The stagnation pressure ahead of the VLS configuration is better predicted by the [19] turbulence model in its BSL variant.

2. Navier-Stokes Equations

The two-dimensional flow is modeled by the Navier-Stokes equations, which express the conservation of mass and energy as well as the momentum variation of a viscous, heat conducting and compressible media, in the absence of external forces. The Navier-Stokes equations are presented in their two-equation turbulence model formulation. The one-equation model is implemented discarding these two-equation models. The integral form of these equations may be represented by:

$$\partial/\partial t \int_V Q dV + \int_S \left[\left(E_e - E_v \right) n_x + \left(F_e - F_v \right) n_y \right] dS + \int_V G dV = 0 , \tag{1}$$

where Q is written for a Cartesian system, V is the cell volume, n_x and n_y are components of the unity vector normal to the cell boundary, S is the flux area, E_e and F_e are the components of the convective, or Euler, flux vector, E_v and F_v are the components of the viscous, or diffusive, flux vector and G is the source term of the two-equation models. The vectors Q, E_e, F_e, E_v and F_v are, incorporating a k-ε or k-ω formulation, represented by:

$$Q = \begin{Bmatrix} \rho \\ \rho u \\ \rho v \\ e \\ \rho k \\ \rho s \end{Bmatrix}, E_e = \begin{Bmatrix} \rho u \\ \rho u^2 + p \\ \rho uv \\ (e+p)u \\ \rho ku \\ \rho su \end{Bmatrix}, F_e = \begin{Bmatrix} \rho v \\ \rho uv \\ \rho v^2 + p \\ (e+p)v \\ \rho kv \\ \rho sv \end{Bmatrix}, E_v = \begin{Bmatrix} 0 \\ t_{xx} + \tau_{xx} \\ t_{xy} + \tau_{xy} \\ f_x \\ \alpha_x \\ \beta_x \end{Bmatrix}; F_v = \begin{Bmatrix} 0 \\ t_{xy} + \tau_{xy} \\ t_{yy} + \tau_{yy} \\ f_y \\ \alpha_y \\ \beta_y \end{Bmatrix}, \text{ and } G = \begin{Bmatrix} 0 \\ 0 \\ 0 \\ 0 \\ G_k \\ G_s \end{Bmatrix}, \tag{2}$$

where the components of the viscous stress tensor are defined as:

$$\begin{aligned} t_{xx} &= \left[2\mu_M \, \partial u/\partial x - 2/3 \mu_M \left(\partial u/\partial x + \partial v/\partial y \right) \right] / Re ; \\ t_{xy} &= \mu_M \left(\partial u/\partial y + \partial v/\partial x \right) / Re ; \\ t_{yy} &= \left[2\mu_M \left(\partial v/\partial y \right) - 2/3 \mu_M \left(\partial u/\partial x + \partial v/\partial y \right) \right] / Re . \end{aligned} \tag{3}$$

The components of the turbulent stress tensor (Reynolds stress tensor) are described by the following expressions:

$$\begin{aligned} \tau_{xx} &= \left[2\mu_T \, \partial u/\partial x - 2/3 \mu_T \left(\partial u/\partial x + \partial v/\partial y \right) \right] / Re - 2/3 \rho k ; \\ \tau_{xy} &= \mu_T \left(\partial u/\partial y + \partial v/\partial x \right) / Re ; \\ \tau_{yy} &= \left[2\mu_T \, \partial v/\partial y - 2/3 \mu_T \left(\partial u/\partial x + \partial v/\partial y \right) \right] / Re - 2/3 \rho k . \end{aligned} \tag{4}$$

Expressions to f_x and f_y are given bellow:

$$f_x = \left(t_{xx} + \tau_{xx} \right) u + \left(t_{xy} + \tau_{xy} \right) v - q_x ; \tag{5}$$

$$f_y = \left(t_{xy} + \tau_{xy} \right) u + \left(t_{yy} + \tau_{yy} \right) v - q_y , \tag{6}$$

where q_x and q_y are the Fourier heat flux components and are given by:

$$q_x = -\gamma / Re \left(\mu_M / Pr_L + \mu_T / Pr_T \right) \partial e_i / \partial x ; \tag{7}$$

$$q_y = -\gamma / Re \left(\mu_M / Pr_L + \mu_T / Pr_T \right) \partial e_i / \partial y . \tag{8}$$

The diffusion terms related to the k-s equations are defined as:

$$\begin{aligned} \alpha_x &= 1/Re \left(\mu_M + \mu_T / \sigma_k \right) \partial k / \partial x ; \\ \alpha_y &= 1/Re \left(\mu_M + \mu_T / \sigma_k \right) \partial k / \partial y ; \end{aligned} \tag{9}$$

$$\beta_x = 1/\mathrm{Re}\left(\mu_M + \mu_T/\sigma_s\right)\partial s/\partial x;$$
$$\beta_y = 1/\mathrm{Re}\left(\mu_M + \mu_T/\sigma_s\right)\partial s/\partial y. \quad (10)$$

In the above equations, ρ is the fluid density; u and v are Cartesian components of the velocity vector in the x and y directions, respectively; e is the total energy per unit volume; p is the static pressure; k is the turbulence kinetic energy; s is the second turbulent variable, which is the rate of dissipation of the turbulence kinetic energy (k-ε model) or the flow vorticity (k-ω model); the t's are viscous stress components; τ's are the Reynolds stress components; the q's are the Fourier heat flux components; G_k takes into account the production and the dissipation terms of k; G_s takes into account the production and the dissipation terms of s; μ_M and μ_T are the molecular and the turbulent viscosities, respectively; Pr_L and Pr_T are the laminar and the turbulent Prandtl numbers, respectively; σ_k and σ_s are turbulence coefficients; γ is the ratio of specific heats; Re is the laminar Reynolds number, defined by:

$$\mathrm{Re} = \rho V_{REF} l_{REF}/\mu_M, \quad (11)$$

where V_{REF} is a characteristic flow velocity and l_{REF} is a configuration characteristic length. The internal energy of the fluid, e_i, is defined as:

$$e_i = e/\rho - 0.5\left(u^2 + v^2\right). \quad (12)$$

The molecular viscosity is estimated by the empiric Sutherland formula:

$$\mu_M = bT^{1/2}/\left(1 + S/T\right), \quad (13)$$

where T is the absolute temperature (K), b = 1.458x10^{-6} Kg/(m.s.K$^{1/2}$) and S = 110.4 K, to the atmospheric air in the standard atmospheric conditions ([23]).

The Navier-Stokes equations are dimensionless in relation to the freestream density, ρ_∞, the freestream speed of sound, a_∞, and the freestream molecular viscosity, μ_∞. The system is closed by the state equation for a perfect gas:

$$p = (\gamma - 1)\left[e - 0.5\rho\left(u^2 + v^2\right) - \rho k\right], \quad (14)$$

considering the ideal gas hypothesis. The total enthalpy is given by $H = \left(e + p\right)/\rho$.

The numerical algorithm is described in [4] and the interested reader is encouraged to read this reference to become familiar with the solver. Moreover, the MUSCL approach used to obtain TVD properties and high resolution is also described in [4] and the interested reader is invocated to read this reference. The spatially variable time step is detailed in [4] and is also recommended to read.

3. Turbulence Models

3.1. Sparlat and Allmaras Turbulence Model

The purpose of the [17] one-equation model was overcome the algebraic model limitations and, at the same time, to avoid the difficulties in the implementation of the two-equation models or the Reynolds stress equations. This model employs a transport turbulent viscosity to solve the turbulence scaling. Such model takes naturally into account the turbulence and diffusion histories, which improves its accuracy.

The transport equation to the work turbulent kinematic viscosity is described by:

$$\frac{D\tilde{\nu}}{Dt} = c_{b1}\tilde{S}\tilde{\nu} + \frac{1}{\sigma}\left[\nabla \bullet \left(\left(\nu + \tilde{\nu}\right)\nabla\tilde{\nu}\right) + c_{b2}\left(\nabla\tilde{\nu}\right)^2\right] - c_{w1}f_w(r)\left(\frac{\tilde{\nu}}{N}\right)^2. \quad (15)$$

In this equation, the first term of the right-hand-side is the production contribution to the work kinematic viscosity; the second term is the viscosity diffusion; and the last term is the destruction of the work kinematic viscosity. The turbulent viscosity is defined by:

$$\mu_T = \rho\tilde{\nu}f_{v1}. \quad (16)$$

With the purpose of assuring that $\tilde{\nu}$ becomes equal to $K \times N \times \sqrt{\tau_{xy,w}/\rho_w}$ in the logarithmic layer and in the viscous sub-layer, the f_{v1} damping function is defined by:

$$f_{v1} = \frac{\lambda^3}{\lambda^3 + {c_{v1}}^3} \quad (17)$$

as function of the $\lambda = \tilde{\nu}/\nu$ variable. The $\tilde{S}$ function, representing the deformation work of the mean flow, is determined as follows:

$$\tilde{S} = \left|\frac{\partial u}{\partial y}\right| + \left[\frac{\tilde{\nu}}{(\kappa N)^2}f_{v2}\right], \quad (18)$$

in which f_{v2} has the following expression:

$$f_{v2} = 1 - \frac{\lambda}{1 + \lambda f_{v1}}. \quad (19)$$

The destruction term should disappear at the external region of the boundary layer. [17] purposes the following function to reproduce such behavior:

$$f_w(r) = g\left[\frac{1 + {c_{w3}}^6}{g^6 + {c_{w3}}^6}\right]^{1/6}, \; g = r + c_{w2}\left(r^6 - r\right), \; r = \frac{\tilde{\nu}}{(\kappa N)^2\tilde{S}}, \quad (20)$$

where r is the argument and f_w is a function reaching the value 1.0 at the logarithmic layer and decreasing at the external region. The g function is merely a limiter to prevent

f_w high values. The [17] model constants are:

$$c_{b1} = 0{,}1355,\ c_{b2} = 0{,}622,\ c_{w2} = 0{,}3,\ c_{v1} = 7{,}1,$$
$$\sigma = 2/3,\ c_{w3} = 2{,}0,\ c_{w1} = \frac{c_{b1}}{\kappa^2} + \frac{(1+c_{b2})}{\sigma}. \quad (21)$$

The [2] model is marched in time using a LU-SGS ("Lower-Upper Factorization – Symmetrical Gauss-Seidel") implicit method. Details of the implicit implementation in two-dimensions are found in [17]. The extension to three-dimensions is straightforward.

In this work, the term referent to the diffusion of the work kinematic viscosity was not implemented. The studied model considers only the production and dissipation terms of the work kinematic viscosity.

3.2. Jacon and Knight Turbulence Model

In the [18] turbulence model, s= ε. It is necessary to define the dissipation rate, which is decomposed as follows:

$$\varepsilon = \varepsilon_s + \varepsilon_d, \quad (22)$$

where ε_d is the dissipation of the dilatation of the turbulent kinetic energy. The Sarkar model is employed to take into account the compressibility effects:

$$\varepsilon_d = M_t^2 \varepsilon_s \ \text{ and } \ M_t^2 = 2k/a^2, \quad (23)$$

with M_t being the turbulent Mach number. The turbulent viscosity is expressed in terms of k and ε as:

$$\mu_T = Re\, C_\mu\, \rho k^2/\varepsilon. \quad (24)$$

The source term denoted by G in the flow equations has the production and dissipation terms of k and ε. To the model of [18], the terms G_k and G_ε have the following expressions:

$$G_k = P_k + D_k \ \text{ and } \ G_\varepsilon = P_\varepsilon + D_\varepsilon, \quad (25)$$

where:

$$P_k = -\tau_{xx}\,\partial u/\partial x - \tau_{xy}(\partial u/\partial y + \partial v/\partial x) - \tau_{yy}\,\partial v/\partial y;\ D_k = \rho\varepsilon; \quad (26)$$

$$P_\varepsilon = C_{\varepsilon 1} P_k\, \varepsilon/k;\ D_\varepsilon = C_{\varepsilon 2}\rho\, \varepsilon_s^2/k. \quad (27)$$

The closure coefficients of the [18] model assume the following values: $C_{\varepsilon 1} = 1.44$, $C_{\varepsilon 2} = 1.92$, $C_\mu = 0.09$, $\sigma_k = 1.0$, $\sigma_\varepsilon = 1.3$, $Pr_L = 0.72$ and $Pr_T = 0.89$.

3.3. Menter and Rumsey Turbulence Model

The [19] model presents four variants: k-ω model of Wilcox, k-ε of two layers, BSL model of [28], and SST (Shear Stress Transport) model of [28]. They are defined as follows:

k-ω model of Wilcox. Constants of the k-ω model of [29]:

$\beta_1^* = 0.09$, $\sigma_1^* = 0.5$, $\kappa_1 = 0.41$, $\gamma_1 = 5/9$, $\sigma_1 = 0.5$ and

$$\beta_1 = \left(\gamma_1 + \sigma_1\kappa_1^2/\sqrt{\beta_1^*}\right)\beta_1^*;$$

Constants of the standard k-ε model of [30]:

$C_\mu = 0.09$, $C_{\varepsilon 1} = 1.44$, $C_{\varepsilon 2} = 1.92$, σk = 1.0, and σε = 1.17;

Constants of the equivalent k-ε model:

$$\beta_2^* = C_\mu,\ \sigma_2^* = 1/\sigma_k,\ \kappa_2 = 0.41,\ \gamma 2 = C_{\varepsilon 1} - 1.0,$$
$$\sigma_2 = 1/\sigma_\varepsilon, \text{ and } \beta_2 = (C_{\varepsilon 2} - 1.0)C_\mu;$$

Weighting function, F_1:

$$F_1 = 1.0;$$

Turbulent viscosity:

$$\mu_T = Re\,\rho k/\omega; \quad (28)$$

k-ε model of two layers. Constants of the k-ω model of [29]:

$\beta_1^* = 0.09$, $\sigma_1^* = 0.5$, $\kappa_1 = 0.41$, $\gamma_1 = 5/9$, $\sigma_1 = 0.4$ and

$$\beta_1 = \left(\gamma_1 + \sigma_1\kappa_1^2/\sqrt{\beta_1^*}\right)\beta_1^*;$$

Constants of the equivalent k-ε model:

$\beta_2^* = 0.09$, $\sigma_2^* = 1.0$, $\kappa_2 = 0.41$, $\gamma 2 = 0.44$, $\sigma_2 = 0.857$, and

$$\beta_2 = \left(\gamma_2 + \sigma_2\kappa_2^2/\sqrt{\beta_2^*}\right)\beta_2^*;$$

Weighting function, F_1:

Γ_1 parameter:

$$\Gamma_1 = 500\upsilon_M/(n^2\omega), \quad (29)$$

with: $\upsilon_M = \mu_M/\rho$ and n = normal distance from the wall to the cell under study;

Coefficient $CD_{k\text{-}\omega}$:

$$CD_{k-\omega} = MAX\left[\left(2\rho\sigma_2/\omega\frac{\partial k}{\partial y}\frac{\partial \omega}{\partial y}\right)/Re,\ 10^{-20}\right]; \quad (30)$$

Γ_2 parameter:

$$\Gamma_2 = 4\rho\sigma_2 k/(n^2 CD_{k-\omega}); \quad (31)$$

Γ_M parameter:

$$\Gamma_M = MIN(\Gamma_1, \Gamma_2); \quad (32)$$

$$F_1 = TANH(\Gamma_M^4); \quad (33)$$

Turbulent viscosity:

$$\mu_T = Re\,\rho k/\omega; \quad (34)$$

Menter's BSL model. Constants of the k-ω model of [29]:

$\beta_1^* = 0.09$, $\sigma_1^* = 0.5$, $\kappa_1 = 0.41$, $\gamma_1 = 5/9$, $\sigma_1 = 0.5$ and

$$\beta_1 = \left(\gamma_1 + \sigma_1\kappa_1^2 \Big/ \sqrt{\beta_1^*}\right)\beta_1^*;$$

Constants of the equivalent k-ε model:

$\beta_2^* = 0.09$, $\sigma_2^* = 1.0$, $\kappa_2 = 0.41$, $\gamma 2 = 0.44$, $\sigma_2 = 0.857$, and

$$\beta_2 = \left(\gamma_2 + \sigma_2\kappa_2^2 \Big/ \sqrt{\beta_2^*}\right)\beta_2^*;$$

Weighting function, F_1:

Γ_1 parameter:

$$\Gamma_1 = 500\upsilon_M / \left(n^2\omega\right);$$

Coefficient $CD_{k-\omega}$:

$$CD_{k-\omega} = MAX\left[\left(2\rho\sigma_2 / \omega \frac{\partial k}{\partial y}\frac{\partial \omega}{\partial y}\right) \Big/ Re,\ 10^{-20}\right];$$

Γ_2 parameter:

$$\Gamma_2 = 4\rho\sigma_2 k / \left(n^2 CD_{k-\omega}\right);$$

Γ_3 parameter:

$$\Gamma_3 = \sqrt{k} / \left(\beta_1^* \omega n\right); \quad (35)$$

Γ_M parameter:

$$\Gamma_M = MIN\left[MAX\left(\Gamma_1, \Gamma_3\right), \Gamma_2\right]; \quad (36)$$

$$F_1 = TANH\left(\Gamma_M^4\right);$$

Turbulent viscosity:

$$\mu_T = Re\rho k / \omega; \quad (37)$$

Menter's SST model. Constants of the k-ω model of [29]:

$\beta_1^* = 0.09$, $\sigma_1^* = 0.5$, $\kappa_1 = 0.41$, $\gamma_1 = 5/9$, $\sigma_1 = 0.5$ and

$$\beta_1 = \left(\gamma_1 + \sigma_1\kappa_1^2 \Big/ \sqrt{\beta_1^*}\right)\beta_1^*;$$

Constants of the equivalent k-ε model:

$\beta_2^* = 0.09$, $\sigma_2^* = 1.0$, $\kappa_2 = 0.41$, $\gamma 2 = 0.44$, $\sigma_2 = 0.857$, and

$$\beta_2 = \left(\gamma_2 + \sigma_2\kappa_2^2 \Big/ \sqrt{\beta_2^*}\right)\beta_2^*;$$

Weighting function, F_1:

Γ_1 parameter:

$$\Gamma_1 = 500\upsilon_M / \left(n^2\omega\right);$$

Coefficient $CD_{k-\omega}$:

$$CD_{k-\omega} = MAX\left[\left(2\rho\sigma_2 / \omega \frac{\partial k}{\partial y}\frac{\partial \omega}{\partial y}\right) \Big/ Re,\ 10^{-20}\right];$$

Γ_2 parameter:

$$\Gamma_2 = 4\rho\sigma_2 k / \left(n^2 CD_{k-\omega}\right);$$

Γ_3 parameter:

$$\Gamma_3 = \sqrt{k} / \left(\beta_1^* \omega n\right);$$

Γ_M parameter:

$$\Gamma_M = MIN\left[MAX\left(\Gamma_1, \Gamma_3\right), \Gamma_2\right];$$

$$F_1 = TANH\left(\Gamma_M^4\right);$$

Weighting function, F_2:

Γ_M parameter:

$$\Gamma_M = MIN\left(2\Gamma_3, \Gamma_1\right); \quad (38)$$

$$F_2 = TANH\left(\Gamma_M^2\right); \quad (39)$$

Ω parameter:

$$\Omega = \left|\partial u / \partial y\right|; \quad (40)$$

Turbulent viscosity:

$$\mu_T = \rho MIN\left[k / \omega, a_1 k / \left(\Omega F_2\right)\right] Re, \quad (41)$$

where $a_1 = 0.31$.

With these definitions, each model can determine the following additional constants:

$$\sigma^* = \sigma_1^* F_1 + \left(1 - F_1\right)\sigma_2^*; \quad (42)$$

$$\sigma = \sigma_1 F_1 + \left(1 - F_1\right)\sigma_2; \quad (43)$$

$$\sigma_k = 1/\sigma^* \quad \text{and} \quad \sigma_\omega = 1/\sigma; \quad (44)$$

$$\gamma = \gamma_1 F_1 + (1 - F_1)\gamma_2; \quad (45)$$

$$\beta = \beta_1 F_1 + (1 - F_1)\beta_2; \quad (46)$$

$$\beta^* = \beta_1^* F_1 + (1 - F_1)\beta_2^*. \quad (47)$$

The source term denoted by G in the governing equations contains the production and dissipation terms of k and ω. To the [19] model, the G_k and G_ω terms have the following expressions:

$$G_k = -P_k + D_k \quad \text{and} \quad G_\omega = -P_\omega + D_\omega - Dif_\omega, \quad (48)$$

where:

$$P_k = \mu_T \left(\frac{\partial u}{\partial y} + \frac{\partial v}{\partial x}\right)\frac{\partial u}{\partial y}\Big/ Re\ ;\ D_k = \beta^* \rho k \omega / Re\ ; \quad (49)$$

$$P_\omega = \gamma P_k / \upsilon_T\ ;\ D_\omega = \beta \rho \omega^2 / Re\ ; \quad (50)$$

$$Dif_\omega = (1 - F_1)\frac{2\rho\sigma_2}{\omega}\frac{\partial k}{\partial y}\frac{\partial \omega}{\partial y}\Big/ Re\ , \quad (51)$$

with: $\upsilon_T = \mu_T / \rho$.

3.4. Gibson and Dafa'Alla Turbulence Model

In the [20] turbulence model, k is replaced by q and s = ζ, where the equivalence between k and q is $k = q^2$. This model has two variants based on the works of [30] and [31]. Initially, it is necessary to calculate the turbulent Reynolds number

$$R_t = k^2 / \left(\upsilon_m^2 \zeta\right). \quad (52)$$

The function f_μ is estimated by [30-31] as

$$f_\mu = \begin{cases} e^{\left[\frac{-6}{(1+R_t/50)^2}\right]}, & [30]; \\ 1 - e^{\left(-0.0115 N^+\right)}, & [31], \end{cases} \quad (53)$$

where $N^+ = \sqrt{Re}\sqrt{\frac{\tau_{xy,w}}{\rho_w}}\frac{N}{\upsilon_{M,w}}$ and N is the normal distance from the surface to the cell under study.

The turbulent viscosity is expressed in terms of k and ω as:

$$\mu_T = Re\, C_\mu \rho f_\mu q^3 / 2\zeta\ . \quad (54)$$

To the [20] model, the G_k and G_ζ terms have the following expressions:

$$G_k = -P_q + D_q \quad \text{and} \quad G_\omega = -P_\zeta + D_\zeta\ , \quad (55)$$

where:

$$P_q = \rho \gamma_T \left(\frac{\partial u}{\partial y} + \frac{\partial v}{\partial x}\right)\frac{\partial u}{\partial y}\Big/ Re \quad \text{and} \quad D_k = \rho\, \zeta / Re\ ; \quad (56)$$

$$P_\zeta = \left(\frac{\zeta}{q}\right) C_{z1} f_{z1} P_k \ \text{ and } \ D_\zeta = \rho\left(\frac{\zeta^2}{q} C_{z2} f_{z2} - \xi_1\right)\Big/ Re\ , \quad (57)$$

where:

$$f_{e2} = \begin{cases} 1 - 0.3e^{-R_t^2}, & [30]; \\ 1 - 0.22e^{-R_t^2/36}, & [31]; \end{cases} \quad (58)$$

$$\gamma_t = 0.25 C_\mu f_\mu\ q^2 / \zeta\ ; \quad (59)$$

$$C_{z1} f_{z1} = 2C_{e1} f_{e1} - 1\ ;\ C_{z2} f_{z2} = 2C_{e2} f_{e2} - 1\ ; \quad (60)$$

$$\xi_1 = -2\upsilon_m \left(\zeta / N^2\right) e^{-0.5N^+}\ . \quad (61)$$

where the closure coefficients adopted for the [20] model are defined in Tab. 1.

Table 1. *Closure coefficients.*

Constant	[30]	[31]
σ_q	1.0	1.0
σ_ζ	1.3	1.3
C_μ	0.09	0.09
C_{e1}	1.44	1.35
C_{e2}	1.92	1.80
f_{e1}	1.0	1.0

4. Initial and Boundary Conditions

The initial and boundary conditions to the [17] turbulence model is the same for perfect gas formulation. Details of these conditions can be found in [17; 24-25]. The initial and boundary conditions to the [18-20] turbulence models are detailed in [4; 26].

5. Results

Tests were performed in a Dual Core processor of 2.3GHz and 2.0Gbytes of RAM microcomputer. Three orders of reduction of the maximum residual in the field were considered to obtain a converged solution. The residual was defined as the value of the discretized conservation equation. The entrance or attack angle was adopted equal to zero. The ratio of specific heats, γ, assumed the value 1.4.

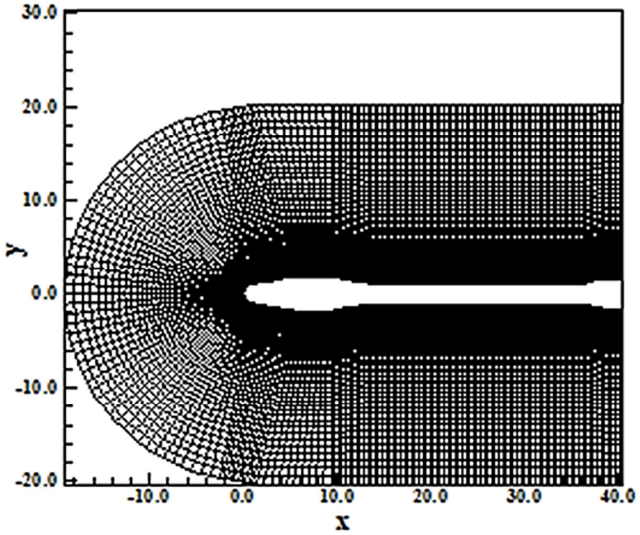

Figure 1. *VLS viscous mesh.*

Figures 1 shows the entire VLS viscous mesh, whereas Fig. 2 shows the detail of the VLS close to the satellite compartment. A mesh of 253x70 points or composed of 17,388 rectangular cells and 17.710 nodes was generated, employing an exponential stretching of 5% in the η direction. The initial data of the simulations are described in Tab. 2.

Table 2. *Initial Conditions.*

M_∞	θ	Altitude	L_∞	Re
3.0	0.0°	40,000m	3.76m	$8.93x10^5$

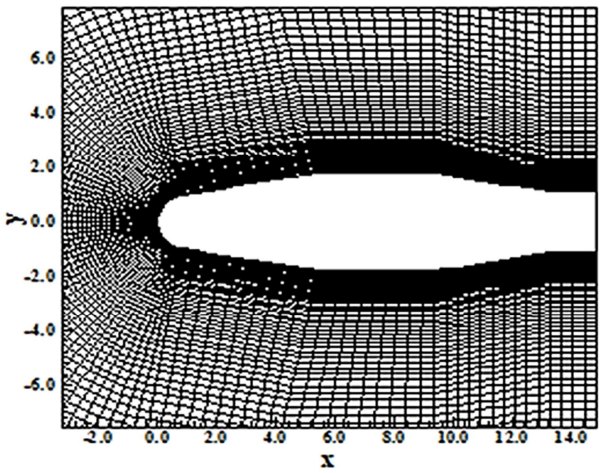

Figure 2. *Detail of the satellite compartment.*

5.1. Sparlat and Allmaras Results

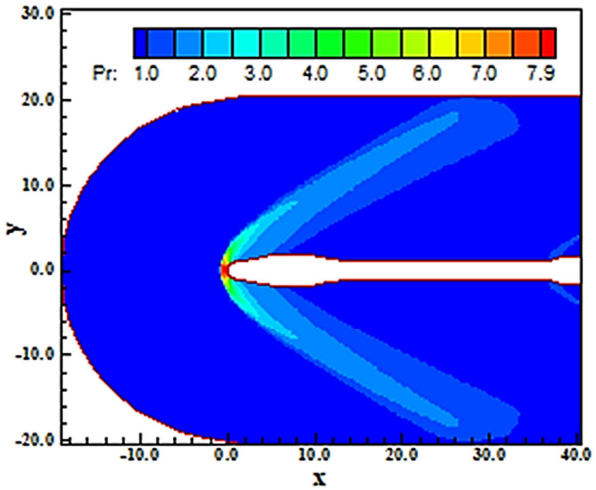

Figure 3. *Pressure contours (SA).*

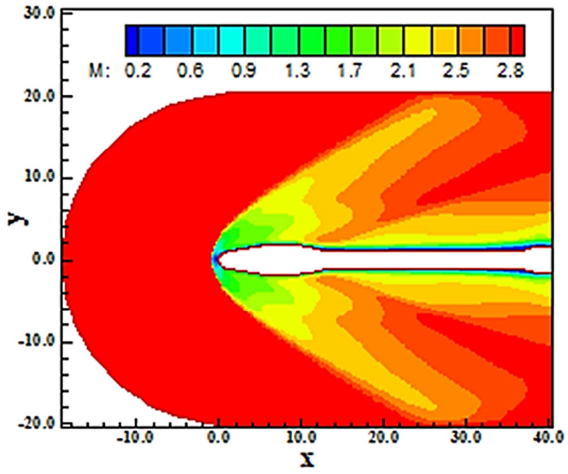

Figure 4. *Mach number contours (SA).*

Figure 3 exhibit the pressure contours obtained by the second order [2] scheme. The contours are uniform and well defined. The normal shock wave at the blunt body nose is well captured. Figure 4 exhibits the Mach number contours obtained by the high resolution TVD [2] scheme. The viscous region close to the VLS walls is well captured; in other words, the heat conduction, through the Fourier law, is well captured by the turbulence model. The normal shock weave is well captured. The solution is free of pre-shock oscillations.

Figure 5 presents the translational/rotational temperature contours obtained by the [2] scheme. Temperatures around 793.0 K are obtained. The region downstream the satellite compartment appears with regions of discrete high dissipation, as can be noted in the figure. In other words, this means that circulation bubbles are formed as consequence of boundary layer displacement. This behavior is also observed at the booster region. These can be seen in Figs. 6 and 7, which highlight the circulation bubble formations downstream the satellite compartment and upstream the booster region. These regions are very discrete, but even so the numerical scheme was able to capture such phenomenon.

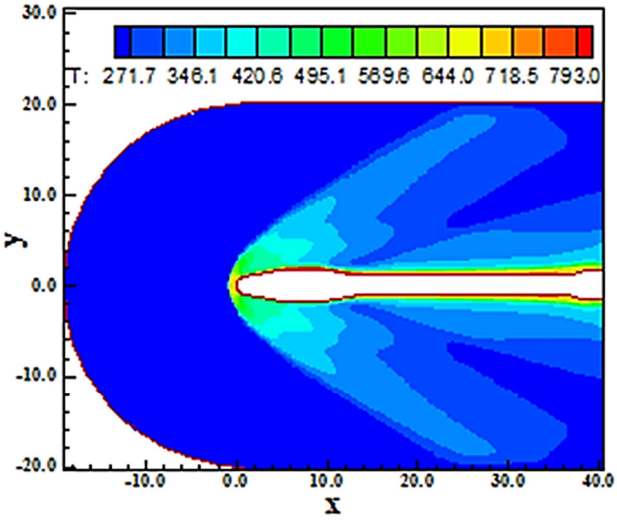

Figure 5. *Temperature contours (SA).*

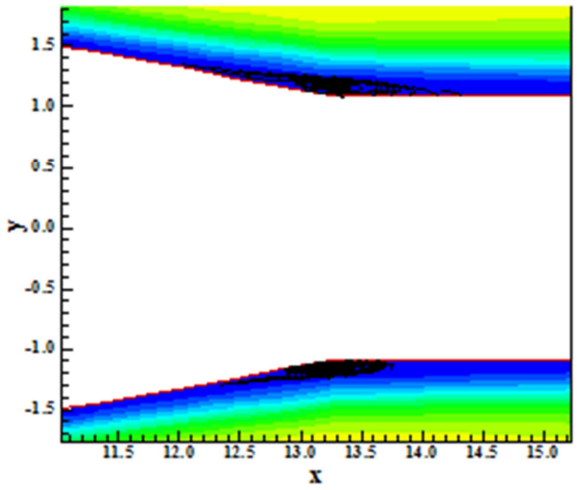

Figure 6. *Circulation bubble formation (Cockpit-SA).*

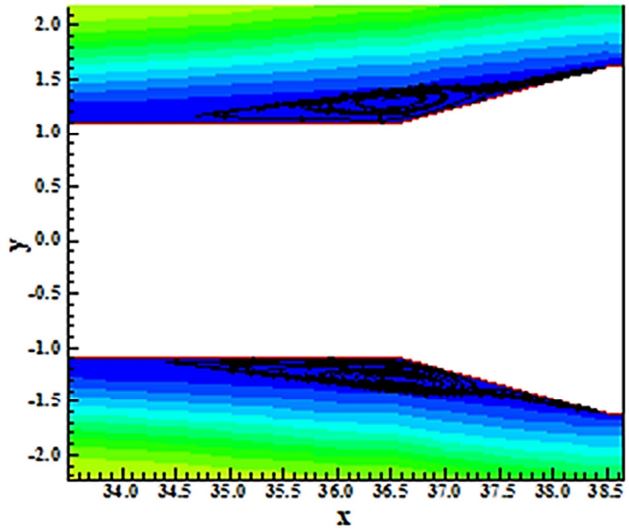

Figure 7. *Circulation bubble formation (Boosters-SA).*

Figure 8 shows the –Cp distribution along the blunt body wall. The –Cp suffers a rapid increase at the satellite compartment and downstream it is horizontal. At the booster region, a rapid decrease in the –Cp values with a recovery pressure at the ramp is observed. In all this distribution, no overshoots and undershoots are perceptible, even for a second-order scheme. This aspect highlights the MUSCL procedure as a good tool to provide clean profiles. Such procedure avoids the appearance of Gibbs phenomenon, typical of second order schemes, yielding good quality solutions.

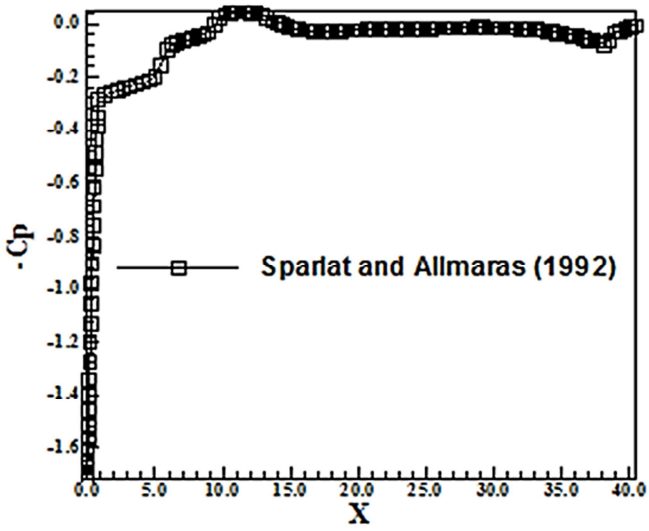

Figure 8. *–Cp distribution (SA).*

5.2. Jacon and Knight Results

Figure 9 shows the pressure contours obtained by the [2] scheme as using the [18] turbulence model. The shock is well defined and homogeneous. As can be seen, there are qualitative differences between this plot and the [17] corresponding plot. The shock at the booster region is captured by both models, but in the [18] turbulence model it is more spread out.

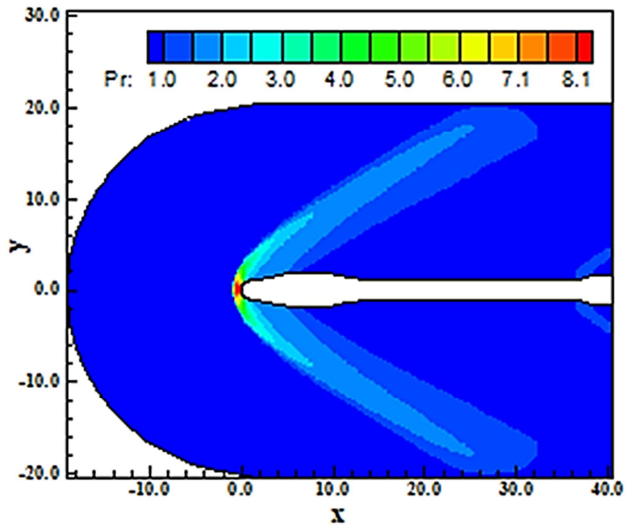

Figure 9. *Pressure contours (JK).*

Figure 10 exhibits the Mach number contours obtained by the [2] numerical scheme as using the [18] turbulence model. The present contours are smoother than the corresponding [17] solution. The normal shock at the blunt nose is well captured by the scheme. The [17] solution is less dissipative than the [18] solution.

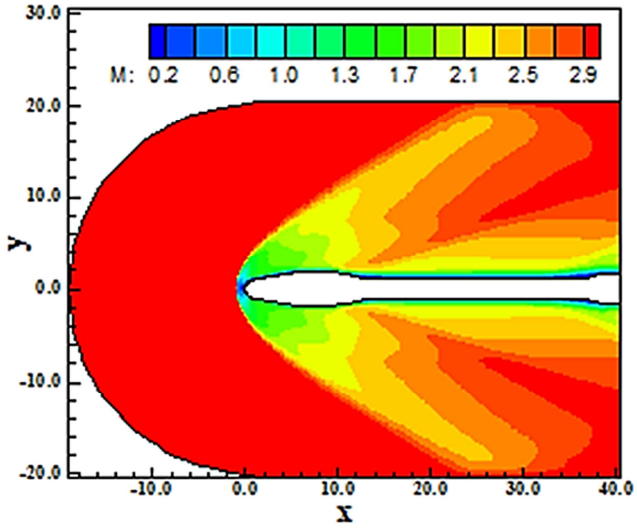

Figure 10. *Mach number contours (JK).*

Figure 11 presents the temperature field obtained by the [2] scheme as using the [18] turbulence model. Qualitatively, this plot has differences in relation to the [17] plot. The [17] solution seems more dissipative. Moreover, the regions of high dissipation are concentrated at the end satellite compartment and at the beginning booster region. Temperatures close to 670.9 K are reached.

Despite the good results, no regions of circulation bubbles are captured by the [18] turbulence model. The satellite compartment end and the booster region beginning are free of

circulation bubble formation, which is a severe penalization to this turbulence model. This separation was captured by all turbulence models of this work and of [4; 26], what becomes improbable its inexistence.

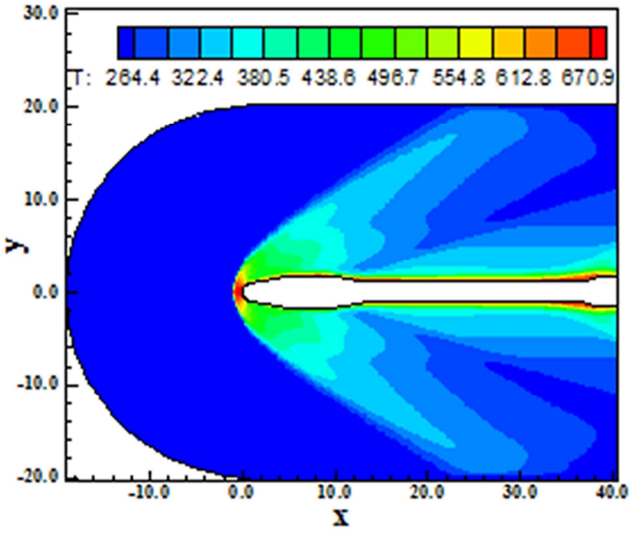

Figure 11. *Temperature contours (JK).*

Figure 12 presents the –Cp distribution at wall of the VLS configuration, generated by the [18] turbulence model. This curve presents a reduction of –Cp close to the booster region and after that the pressure coefficient is recovered at the booster end. The –Cp distribution along the VLS central body is relative smooth, without oscillations in the solution.

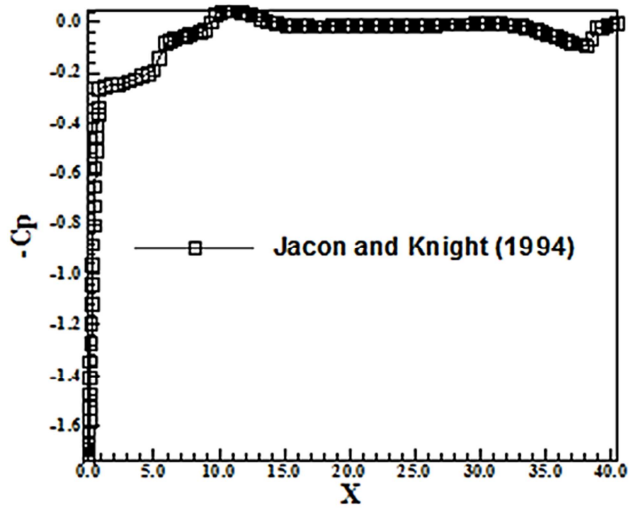

Figure 12. *–Cp distribution (JK).*

5.3. Menter and Rumsey Results

Wilcox Option. Figure 13 shows the pressure contours generated by the [2] scheme as using the [19] turbulence model in its Wilcox variant. This curve is very similar to the [17] and [18] models. The shock is well captured and the solution is homogeneous, without pre-shock oscillations. The oblique shock at the ramp is also well captured by the turbulence model.

Figure 14 exhibits the Mach number contours obtained as using the [19] turbulence model in its Wilcox variant. The solution is very close to the [18] solution. It is possible to note that this solution presents more dissipation than the [17] solution. Regions of discrete formation of separation bubbles are perceptible at the downstream region of the satellite compartment and at the booster region. It is possible to see in Figs. 16 and 17 that circulation bubbles are well formed.

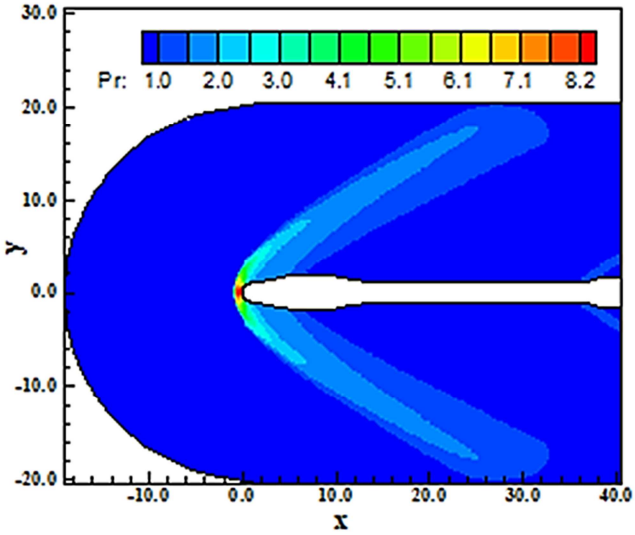

Figure 13. *Pressure contours (MR-W).*

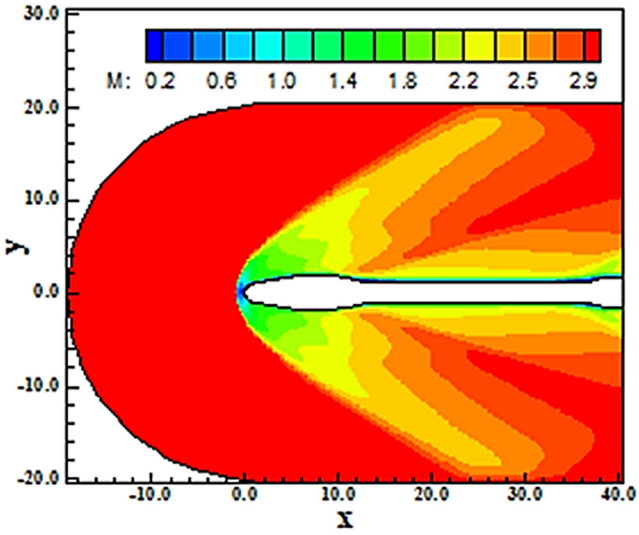

Figure 14. *Mach number contours (MR-W).*

Figure 15 presents the translational temperature contours originated by the [2] scheme as using the [19] turbulence model. Temperatures near 839.3 K are observed in the field, superior to the respective field in the [17] and [18] results.

Figures 16 and 17 corroborate what was observed in the aforementioned paragraph. Circulation bubbles formation is originated at regions of high heating and generate loss of energy by the bubbles displacement and energy exchange due to collisions.

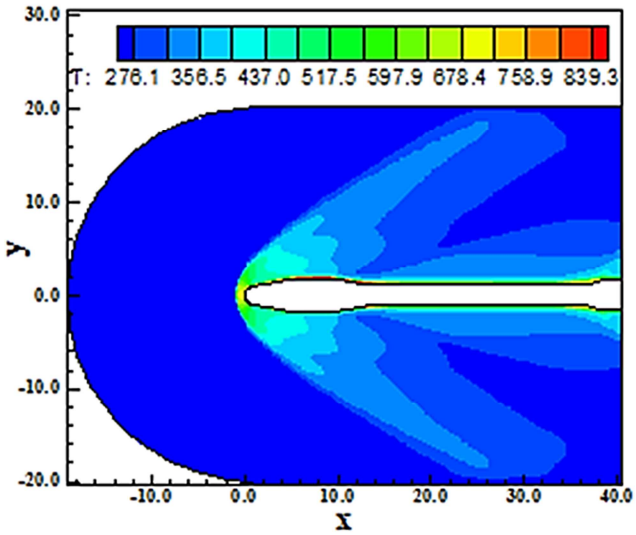

Figure 15. *Temperature contours (MR-W).*

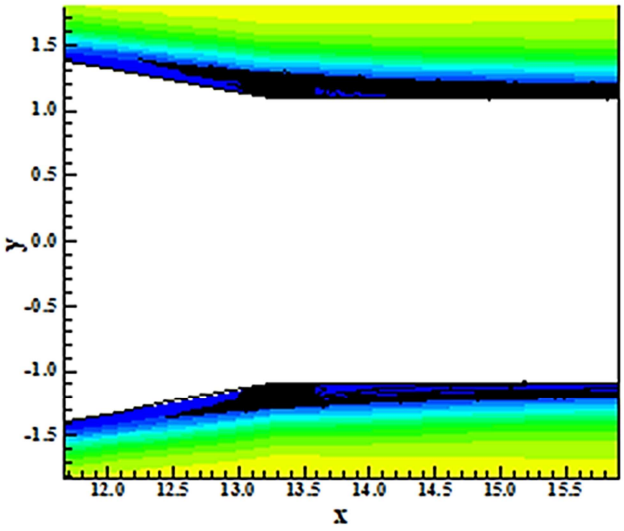

Figure 16. *Circulation bubble formation (Cockpit-MR-W).*

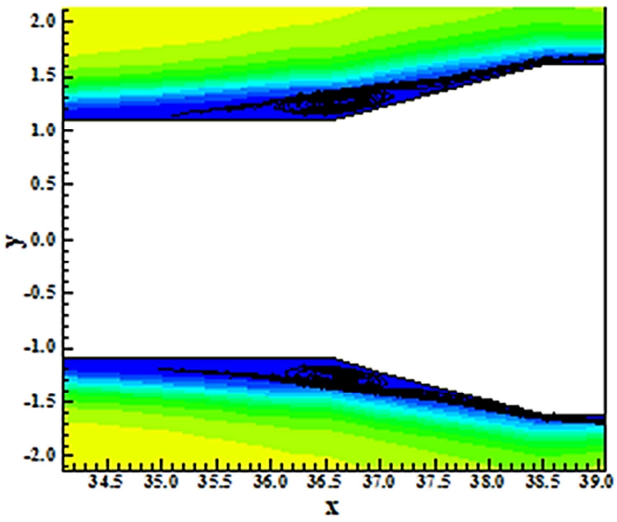

Figure 17. *Circulation bubble formation (Boosters-MR-W).*

Figure 18 exhibits the –Cp distribution originated by the [19] turbulence model. The cockpit region upstream presents a pressure distribution in steps and also presents the reduction of pressure close to the boosters region, with the consequent increase of such pressure, obtained in all other solutions. The –Cp profile is less strength than the –Cp profile of the [17] and [18] turbulence models. However, it is equivalent in qualitative terms in relation to the [18] turbulence model.

Two Layer k-ε Option. Figure 19 shows the pressure contours generated by the [2] scheme as using the [19] turbulence model in its Two Layer variant. This curve is very similar to the [17] model. The shock is well captured and the solution is homogeneous, without pre-shock oscillations.

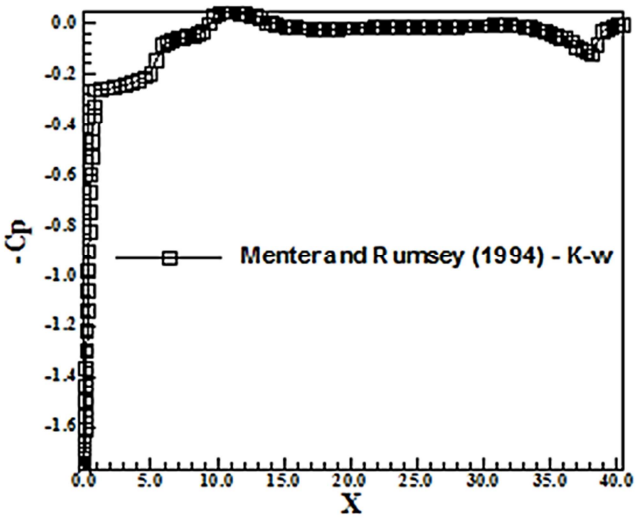

Figure 18. *–Cp distribution (MR-W).*

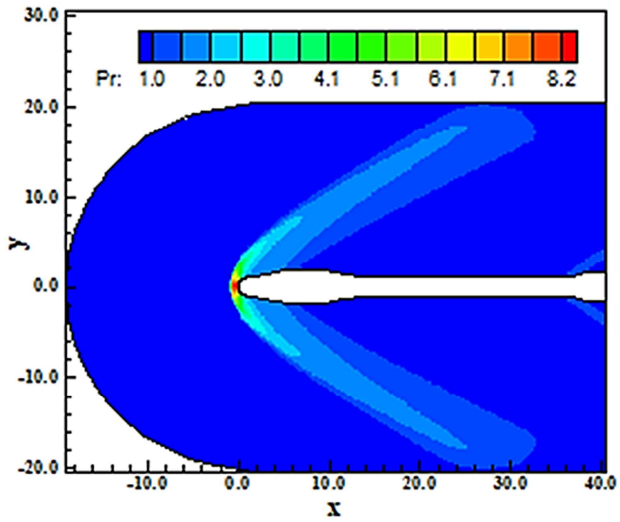

Figure 19. *Pressure contours (MR-TL).*

Figure 20 exhibits the Mach number contours obtained as using the [19] turbulence model in its Two Layer variant. The solution is very close to the [18] solution. It is possible to note that this solution is so dissipative as the [18] solution. Regions of discrete formation of separation bubbles are perceptible at the downstream region of the satellite compartment and at the

booster region. It is possible to see in Figs. 22 and 23 that circulation bubbles are well formed.

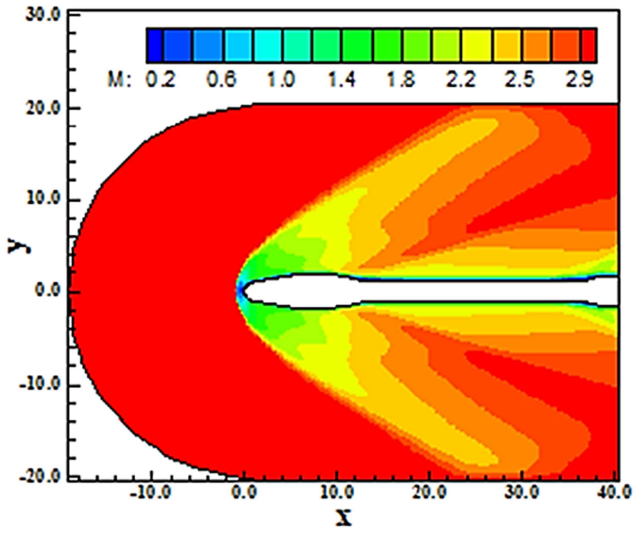

Figure 20. *Mach number contours (MR-TL).*

Figure 21 presents the translational temperature contours originated by the [2] scheme as using the [19] turbulence model. Temperatures near 838.5 K are observed in the field, superior to those observed in [17] and [18] fields. Regions of high temperature are observed at the blunt body nose and at the satellite compartment end.

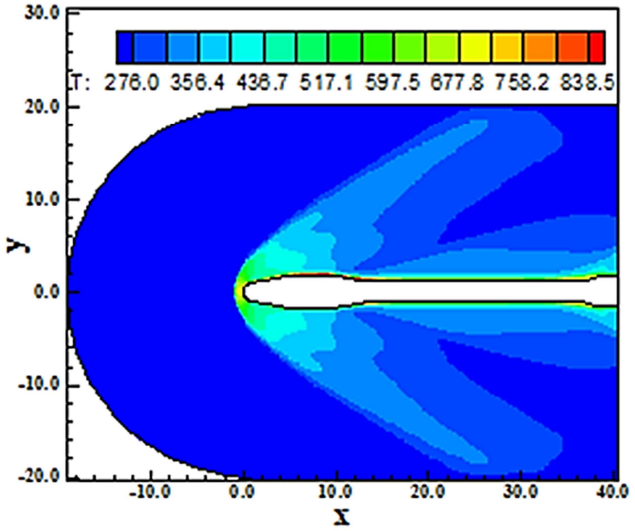

Figure 21. *Temperature contours (MR-TL).*

Figures 22 and 23 show the circulation bubble formation at regions of high heating. Both regions generate loss of energy by the bubbles displacement and energy exchange due to collisions.

Figure 24 exhibits the –Cp distribution originated by the [19] turbulence model. The cockpit region upstream presents a pressure distribution in steps and also presents the reduction of pressure close to the boosters region, with the consequent increase of such pressure, obtained in all other solutions. The –Cp profile is less strength than the –Cp profile of the [17] and [18] turbulence models.

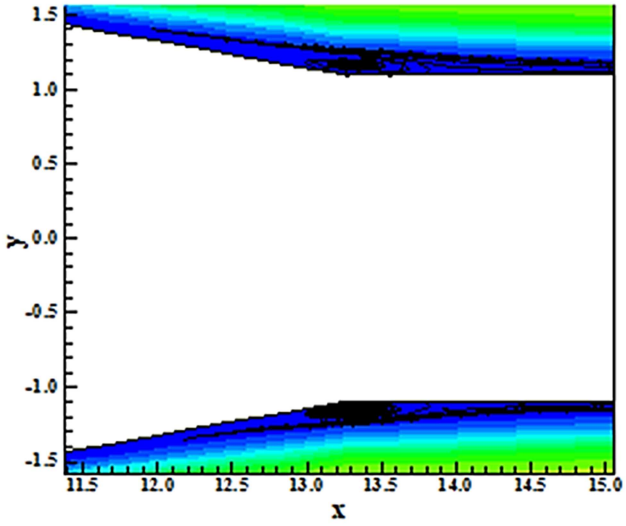

Figure 22. *Circulation bubble formation (Cockpit-MR-TL).*

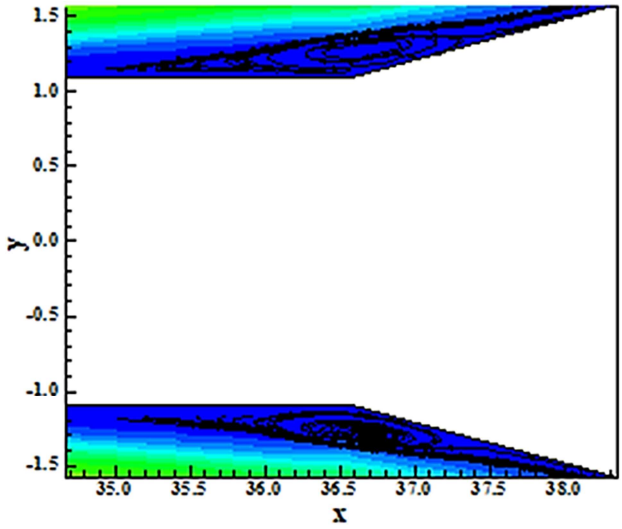

Figure 23. *Circulation bubble formation (Boosters-MR-TL).*

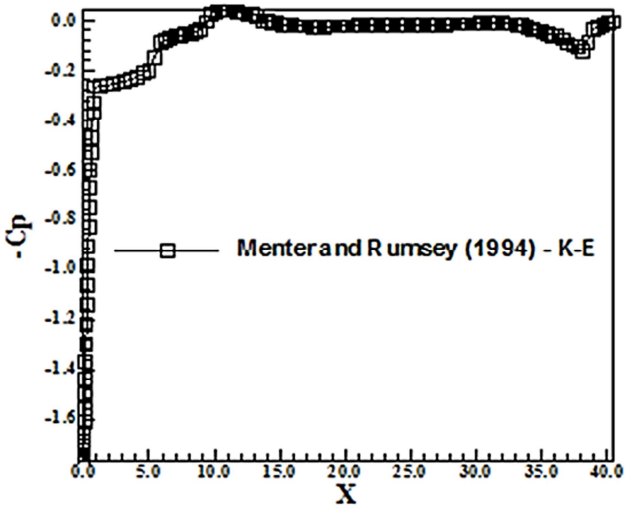

Figure 24. *–Cp distribution (MR-TL).*

However, it is equivalent in qualitative terms in relation to the [17] and [18] turbulence models.

BSL Option. Figure 25 shows the pressure contours generated by the [2] scheme as using the [19] turbulence model in its BSL variant. This curve is very similar to the [17] model. The shock is well captured and the solution is homogeneous, without pre-shock oscillations. The oblique shock wave at the booster beginning is well captured.

Figure 26 exhibits the Mach number contours obtained as using the [19] turbulence model in its BSL variant. The solution is very close to the [18] solution. It is possible to note that this solution present more dissipation than the [17] solution. Regions of discrete formation of separation bubbles are perceptible at the downstream region of the satellite compartment and at the booster region.

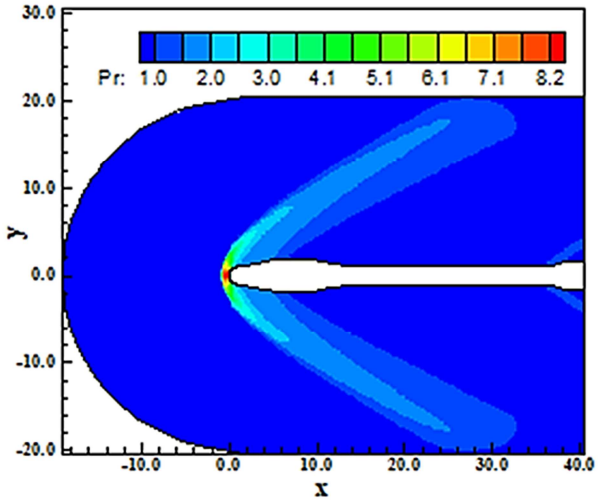

Figure 25. *Pressure contours (MR-BSL).*

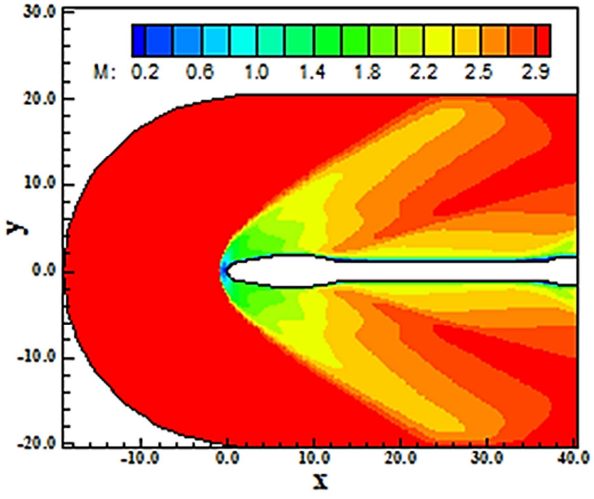

Figure 26. *Mach number contours (MR-BSL).*

Figure 27 presents the translational temperature contours originated by the [2] scheme as using the [19] turbulence model. Temperatures near 839.3 K are observed in the field, superior to the [17] and [18] fields. Regions of high temperature are observed at the blunt body nose and at the satellite compartment end.

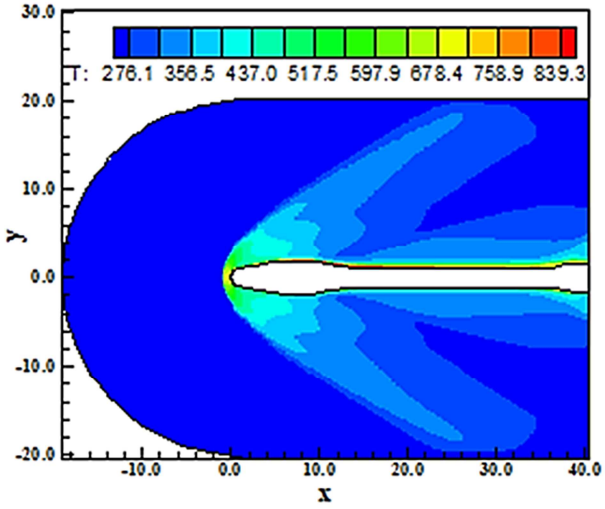

Figure 27. *Temperature contours (MR-BSL).*

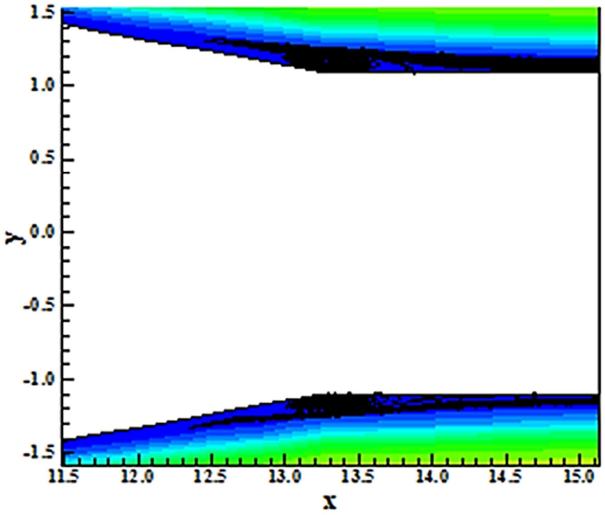

Figure 28. *Circulation bubble formation (Cockpit-MR-BSL).*

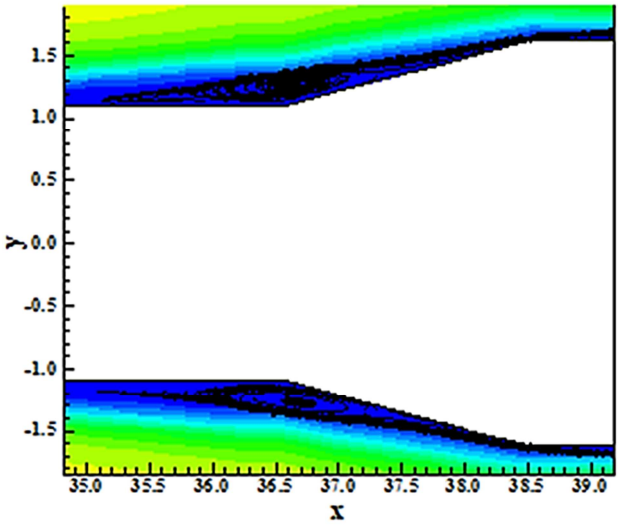

Figure 29. *Circulation bubble formation (Boosters-MR-BSL).*

Figures 28 and 29 show the circulation bubble formation resulting from regions of high heating. These regions generate loss of energy by the bubbles displacement and energy exchange due to collisions.

Figure 30 exhibits the –Cp distribution originated by the [19] turbulence model. The cockpit upstream region presents a pressure distribution in steps and also presents the reduction of pressure close to the boosters region, with the consequent increase of such pressure, obtained in all other solutions. The –Cp profile is less strength than the –Cp profile of the [17] and [18] turbulence models. However, it is equivalent in qualitative terms in relation to the [17] and [18] turbulence models.

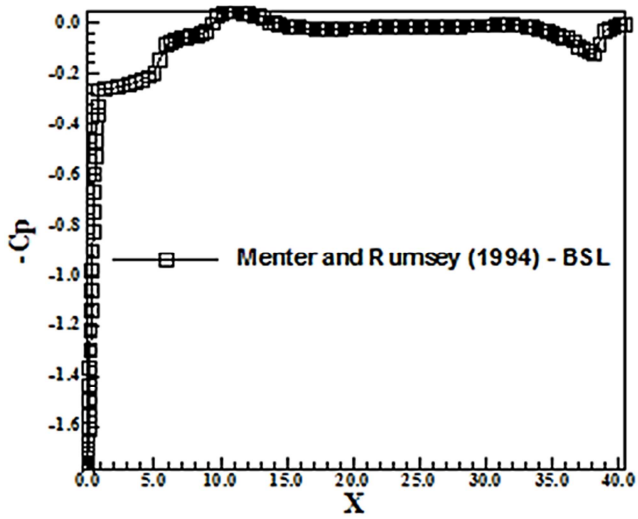

Figure 30. *–Cp distribution (MR-BSL).*

SST Option. Figure 31 shows the pressure contours generated by the [2] scheme as using the [19] turbulence model in its SST variant. This curve is very similar to the [17] and [18] models. It is also very similar with the other contours of the [19] turbulence model.

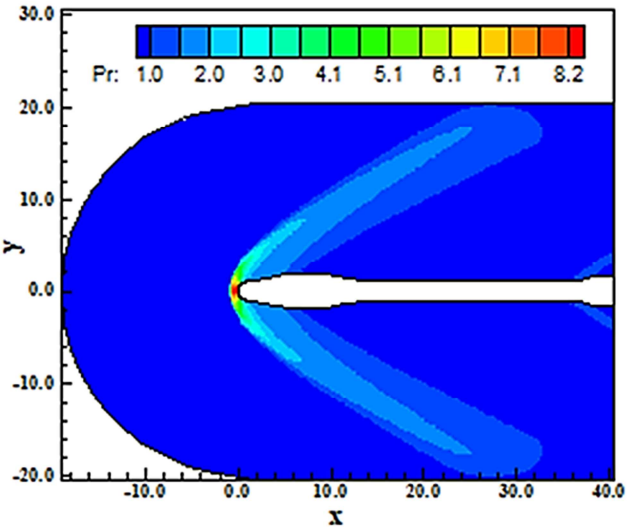

Figure 31. *Pressure contours (MR-SST).*

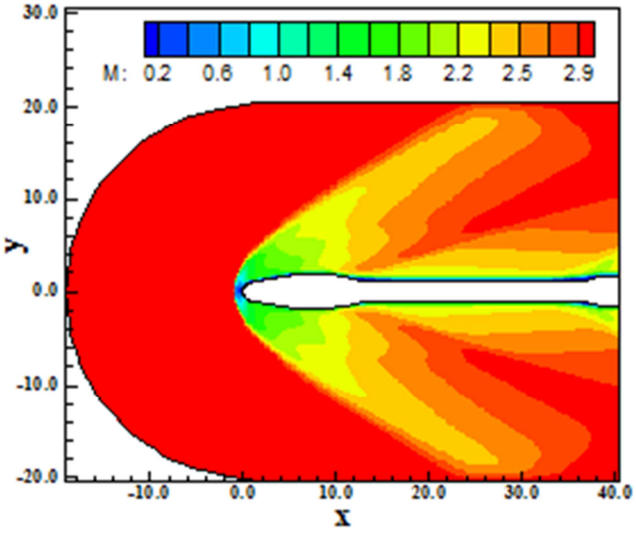

Figure 32. *Mach number contours (MR-SST).*

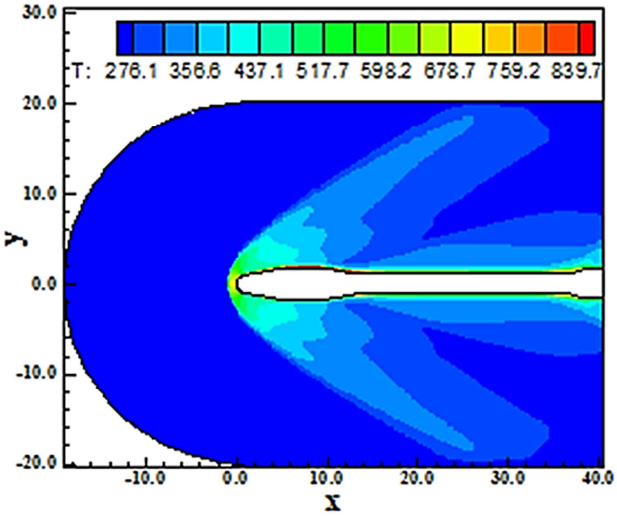

Figure 33. *Temperature contours (MR-SST).*

The shock is well captured and the solution is homogeneous, without pre-shock oscillations. The oblique shock wave at the booster region is also well captured, without excessive spread out.

Figure 32 exhibits the Mach number contours obtained as using the [19] turbulence model in its SST variant. The solution is very close to the [18] solution. It is possible to note that this solution present more dissipation than the [17] solution. Regions of discrete formation of separation bubbles are perceptible at the downstream region of the satellite compartment and at the booster region. It is possible to see in Figs. 34 and 35 that circulation bubbles are well formed.

Figure 33 presents the translational temperature contours originated by the [2] scheme as using the [19] turbulence model. Temperatures near 839.7 K are observed in the field, superior to all other fields in the solutions studied until herein.

Figures 34 and 35 corroborate what was observed in the aforementioned paragraph. Circulation bubbles formation is originated at regions of high heating and generate loss of

energy by the bubbles displacement and energy exchange due to collisions.

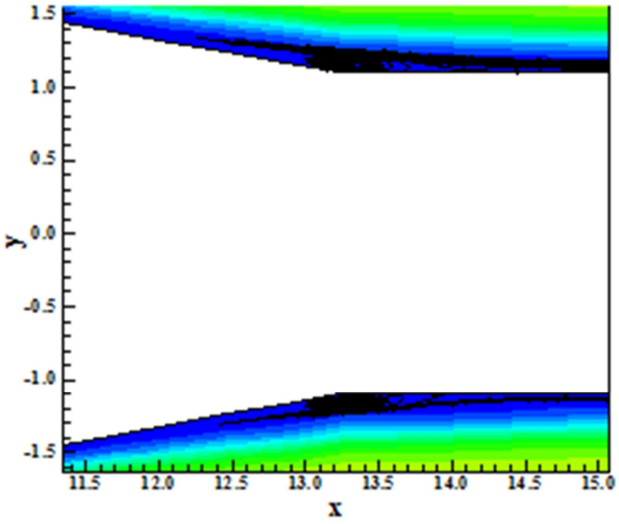

Figure 34. *Circulation bubble formation (Cockpit-MR-SST).*

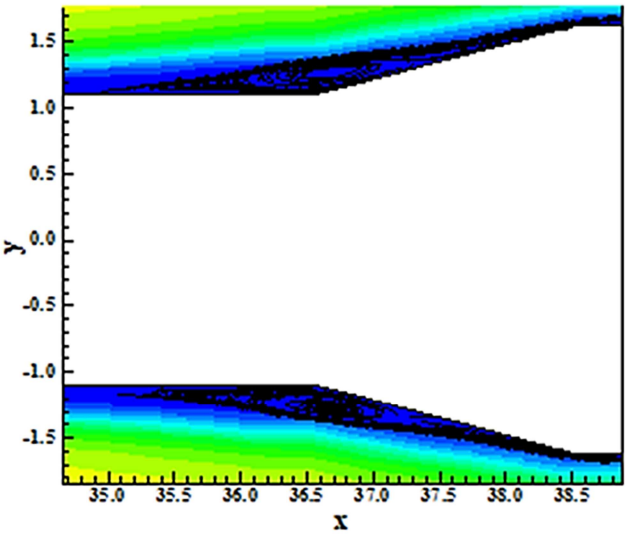

Figure 35. *Circulation bubble formation (Boosters-MR-SST).*

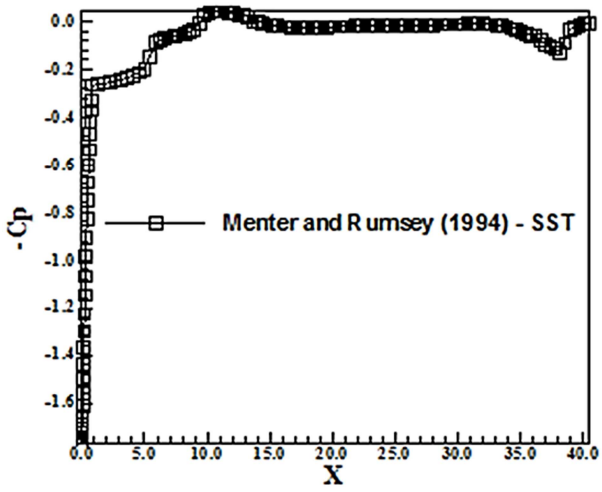

Figure 36. *–Cp distribution (MR-SST).*

Figure 36 exhibits the –Cp distribution originated by the [19] turbulence model. The cockpit upstream region presents a pressure distribution in steps and also presents the reduction of pressure close to the booster regions, with the consequent increase of such pressure, obtained in all other solutions. The –Cp profile of the SST turbulence model is less strength than the –Cp profile of the [17] and [18] turbulence models. However, it is equivalent in qualitative terms in relation to the [17] and [18] turbulence models.

5.4. Gibson and Dafa'Alla Results

Launder and Sharma Option to Constants and f_μ. Figure 37 shows the pressure contours obtained by the [2] algorithm as the [20] turbulence model, in its LS-LS variant, is employed. The contour curves are well defined and the solution quality is the same as in the [17] solution. The shock at the booster region is well captured. No overshoots or undershoots are present, corroborating the idea of this scheme prevents Gibbs phenomenon.

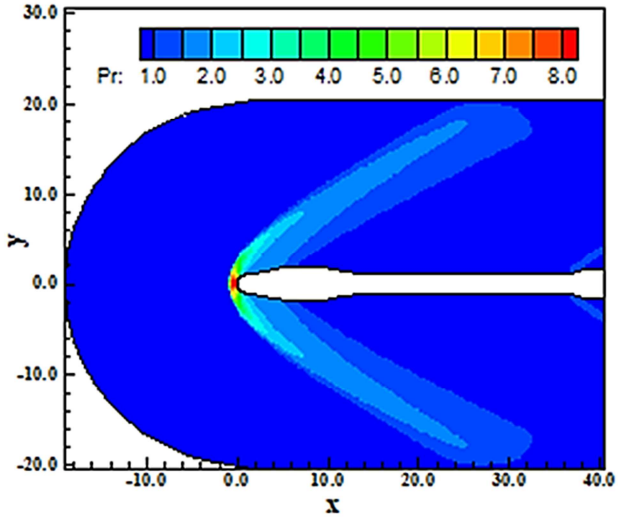

Figure 37. *Pressure contours (GA-LSLS).*

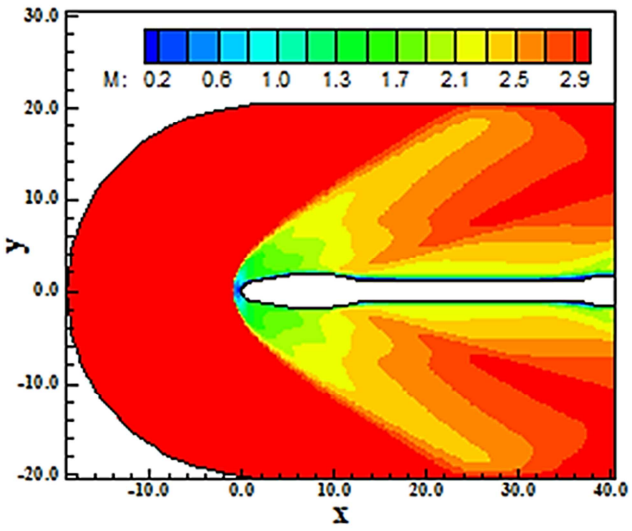

Figure 38. *Mach number contours (GA-LSLS).*

Figure 38 exhibits the Mach number contours obtained by the [20] turbulence model in its LS-LS variant. The contours present more dissipative features than the [17] contours. No pre-shock oscillations are perceptible. The subsonic region is formed at the blunt nose as expected.

Figure 39 presents the translational temperature contours originated from the [20] turbulence model. The temperature peak is observed near to 697.0 K, which is less than the [19] captured field and close to the [18-19] captured fields. It is possible to detect regions of great heating near the satellite compartment end and at the booster regions. Corroborating this observation, circulation bubble formations were detected in these regions. Figures 40 and 41 show these regions. They are discrete, but observable, and ratifies the expected behavior.

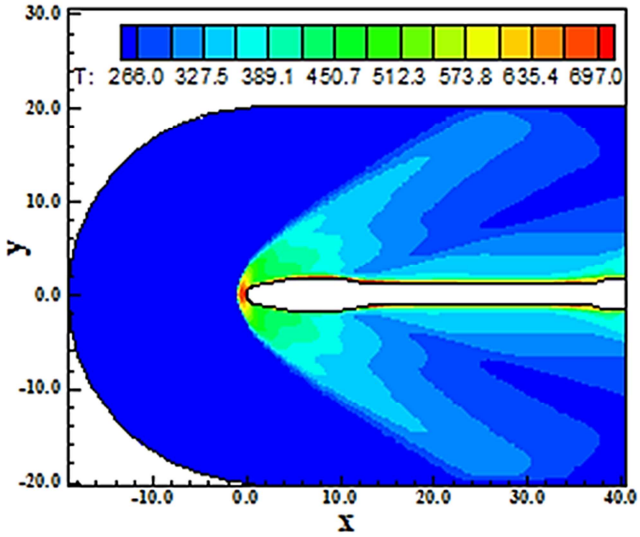

Figure 39. *Temperature contours (GA-LSLS).*

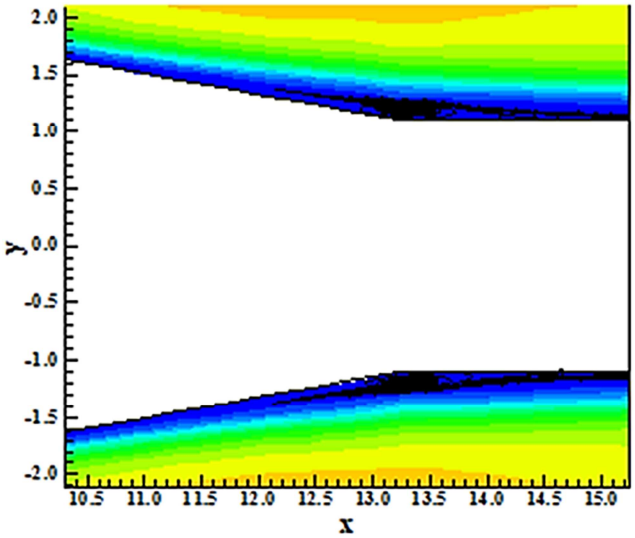

Figure 40. *Circulation bubble formation (Cockpit-GA-LSLS).*

Figure 42 shows the –Cp distribution obtained with the [20] turbulence model. The step profile at the blunt nose region and the hole region at the booster region are again observable. The pressure recovery at the booster region is typical of all solutions in this study. This –Cp profile is not so strength than the [17] and [18] profiles.

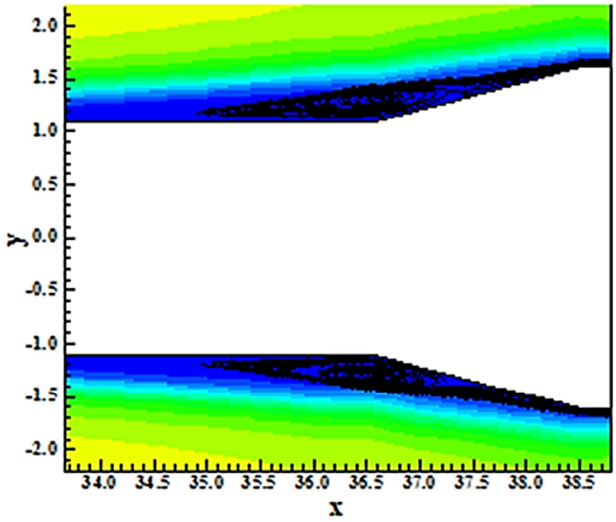

Figure 41. *Circulation bubble formation (Boosters-GA-LSLS).*

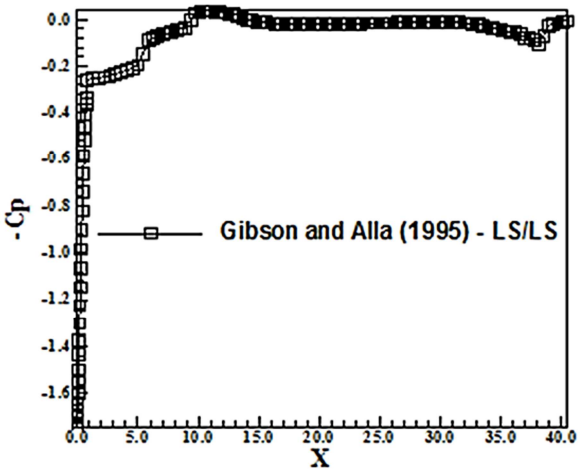

Figure 42. *–Cp distribution (GA-LSLS).*

Launder and Sharma Option to Constants and Chien to f_μ. Figure 43 shows the pressure contours obtained by the [2] algorithm as the [20] turbulence model, in its LS-C variant, is employed. The contour curves are well defined and the solution quality is the same as in the [17] and [19] solutions. The shock at the booster region is well captured. No overshoots or undershoots are present, corroborating the idea of this scheme prevents Gibbs phenomenon.

Figure 44 exhibits the Mach number contours obtained by the [20] turbulence model in its LS-C variant. The contours present more dissipative features than the [17] contours. No pre-shock oscillations are perceptible. The subsonic region is formed at the blunt nose as expected.

Figure 45 presents the translational temperature contours originated from the [20] turbulence model. The temperature

peak is observed near to 698.4 K, which is less than the [19] captured field and close to the [17-18] captured fields.

It is possible to detect regions of great heating near the satellite compartment end and at the booster regions.

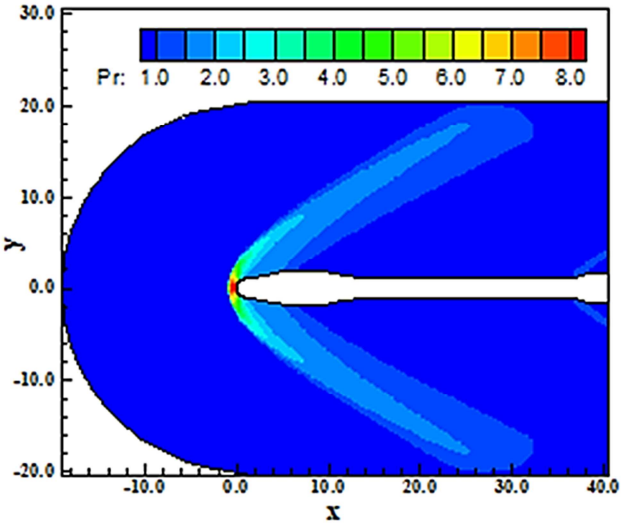

Figure 43. *Pressure contours (GA-LSC).*

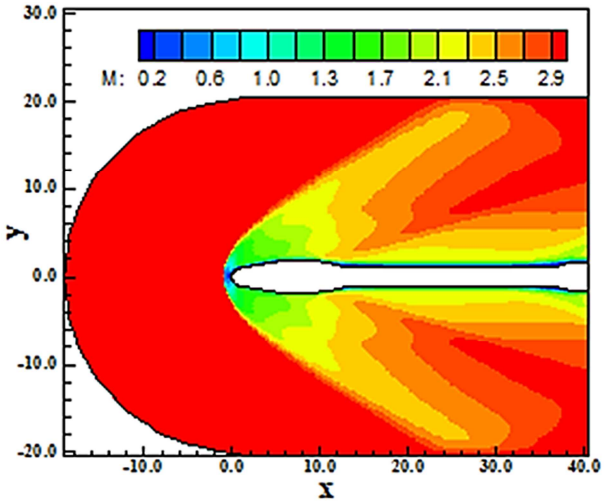

Figure 44. *Mach number contours (GA-LSC).*

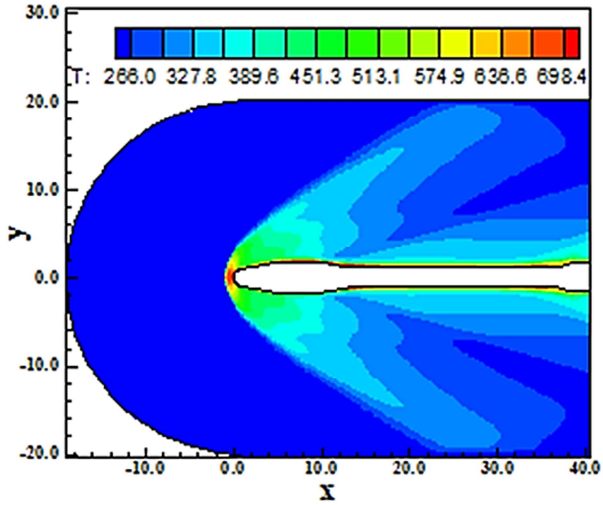

Figure 45. *Temperature contours (GA-LSC).*

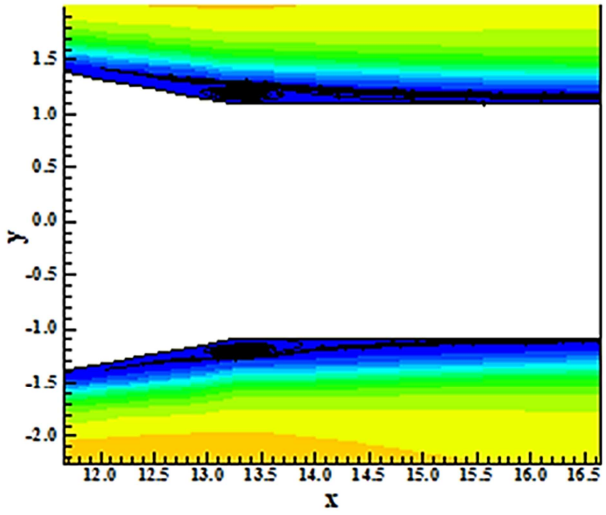

Figure 46. *Circulation bubble formation (Cockpit-GA-LSC).*

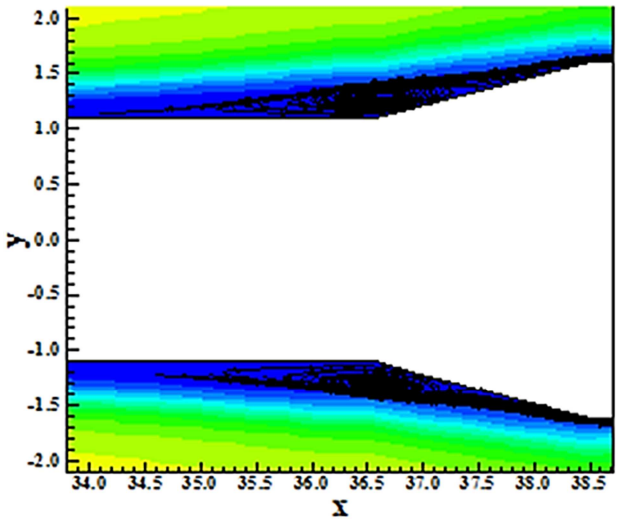

Figure 47. *Circulation bubble formation (Boosters-GA-LSC).*

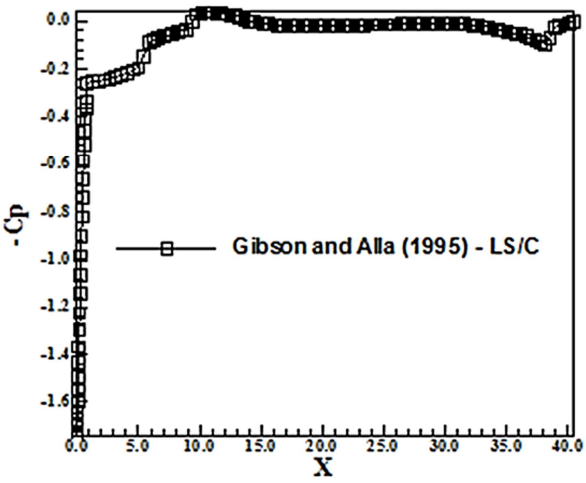

Figure 48. *–Cp distribution (GA-LSC).*

Confirming this observation, circulation bubble formations were detected in these regions. Figures 46 and 47 show these regions. They are discrete, but observable, and ratifies the expected behavior.

Figure 48 shows the –Cp distribution obtained with the [20] turbulence model. The step profile at the blunt nose region and the hole region at the booster region are again observable. The pressure recovery at the booster region is typical of all solutions in this study. This –Cp profile is not so strength than the [17] and [18] profiles.

Chien Option to Constants and Launder and Sharma to f_μ. Figure 49 shows the pressure contours obtained by the [2] algorithm as the [20] turbulence model, in its C-LS variant, is employed. The curves of contours are well defined and the solution quality is the same as in the [17] and [19] solutions. The shock at the booster region is well captured, without excessive spread out. No overshoots or undershoots are present.

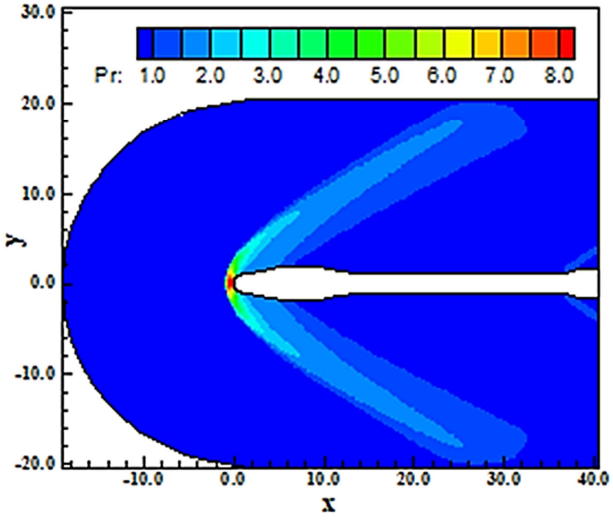

Figure 49. *Pressure contours (GA-CLS).*

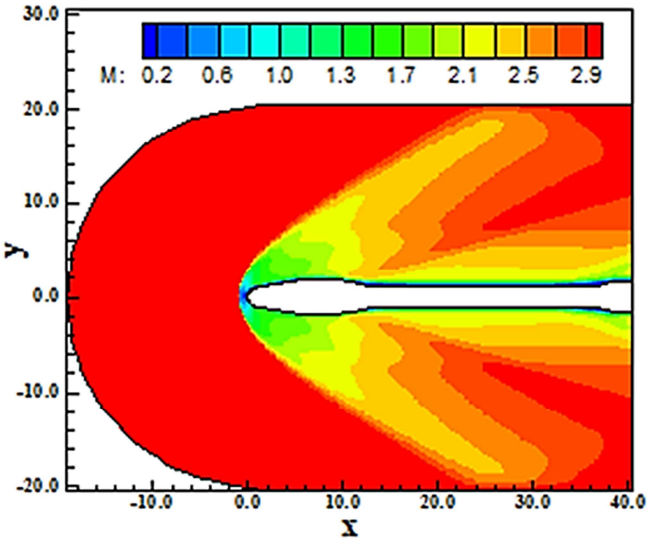

Figure 50. *Mach number contours (GA-CLS).*

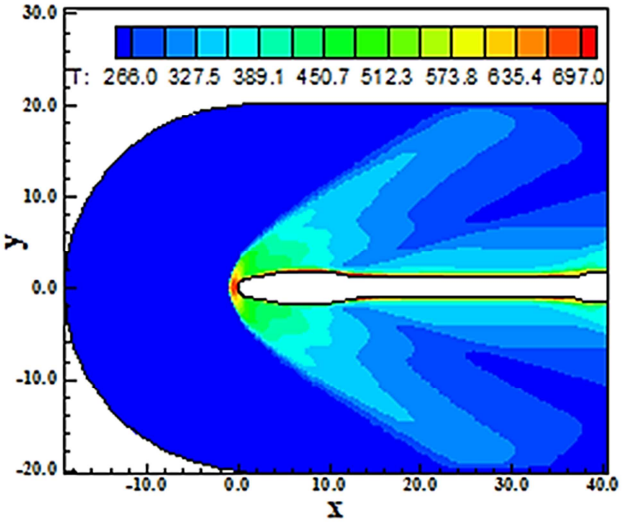

Figure 51. *Temperature contours (GA-CLS).*

Figure 50 exhibits the Mach number contours obtained by the [20] turbulence model in its C-LS variant. The contours present more dissipative features than the [17] contours. No pre-shock oscillations are perceptible. The subsonic region is formed at the blunt nose as expected.

Figure 51 presents the translational temperature contours originated from the [20] turbulence model. The temperature peak is observed near to 697.0 K, which is less than the [19] captured field and close to the [17-18] captured fields. It is possible to detect regions of great heating near the satellite compartment end and at the booster regions. Confirming this observation, circulation bubble formations were detected in these regions. Figures 52 and 53 show these regions. They are discrete, but observable, and ratifies the expected behavior.

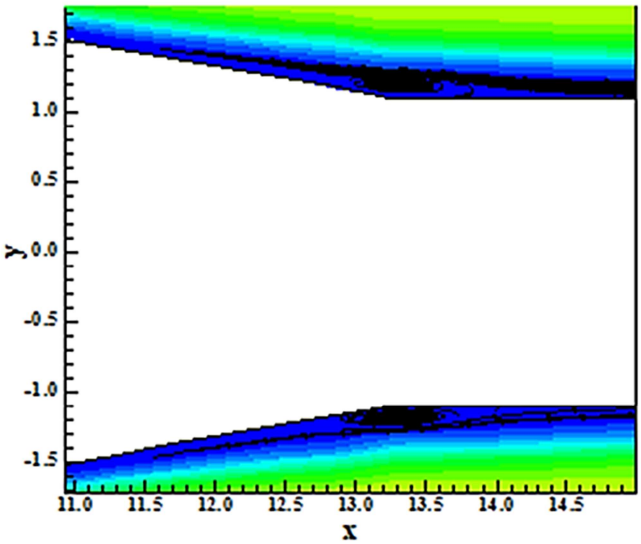

Figure 52. *Circulation bubble formation (Cockpit-GA-CLS).*

Figure 54 shows the –Cp distribution obtained with the [20] turbulence model. The step profile at the blunt nose region and the hole region at the booster region are again observable. The

pressure recovery at the booster region is typical of all solutions in this study. This –Cp profile is not so strength than the [17] and [18] profiles. The central region of the –Cp distribution is quasi horizontal, highlighting a constant –Cp region.

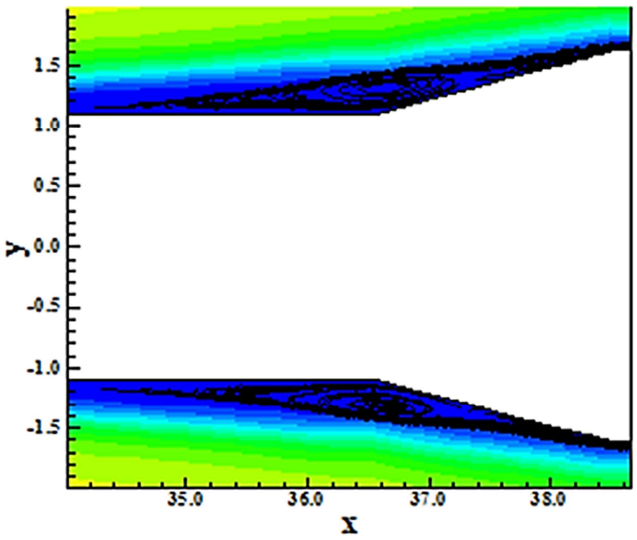

Figure 53. *Circulation bubble formation (Boosters-GA-CLS).*

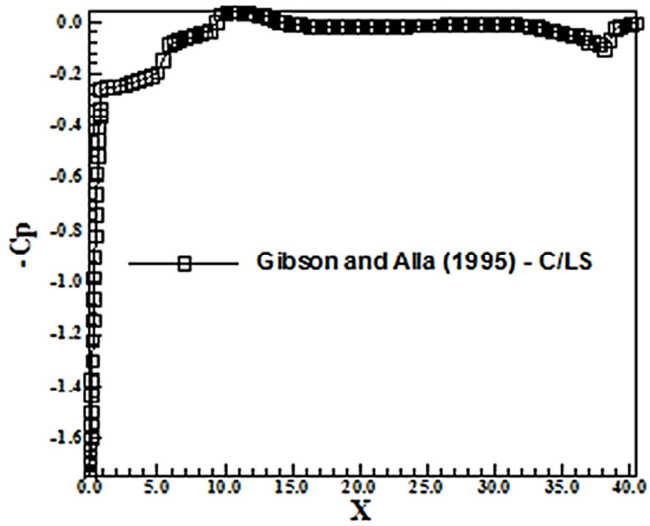

Figure 54. *–Cp distribution (GA-CLS).*

Chien Option to Constants and f_μ. Figure 55 shows the pressure contours obtained by the [2] algorithm as the [20] turbulence model, in its C-C variant, is employed. The contour curves are well defined and the solution quality is the same as in the [17] and [19] solutions. The shock at the booster region is well captured. No overshoots or undershoots are present, corroborating the idea of this scheme prevents Gibbs phenomenon.

Figure 56 exhibits the Mach number contours obtained by the [20] turbulence model in its C-C variant. The contours present more dissipative features than the [17] contours. No pre-shock oscillations are perceptible. The subsonic region is formed at the blunt nose as expected.

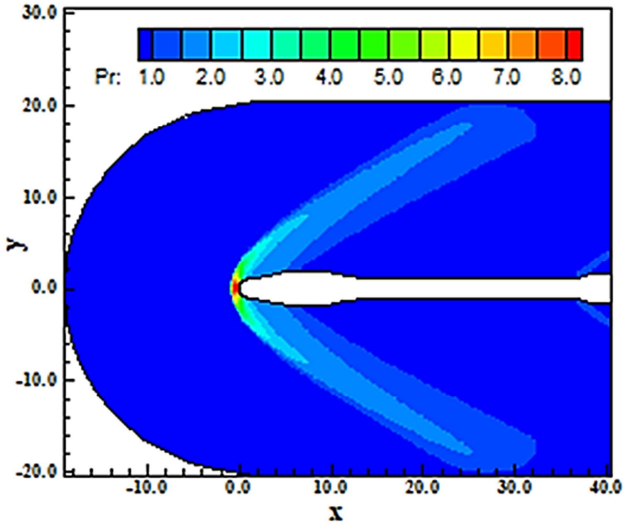

Figure 55. *Pressure contours (GA-CC).*

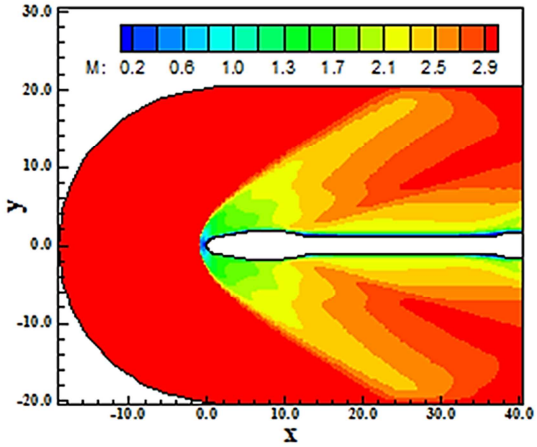

Figure 56. *Mach number contours (GA-CC).*

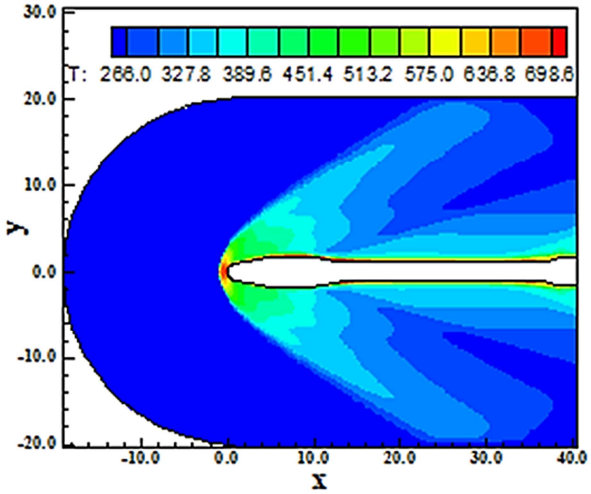

Figure 57. *Temperature contours (GA-CC).*

Figure 57 presents the translational temperature contours originated from the [20] turbulence model. The temperature peak is observed near to 698.6 K, which is less than the [19] captured field and close to the [17-18] capture fields. Regions

of great heating near the satellite compartment end or at the booster regions are detected. Ratifying this observation, circulation bubble formations were detected in these regions. Figures 58 and 59 show these regions. They are discrete, but observable, and corroborate the expected behavior.

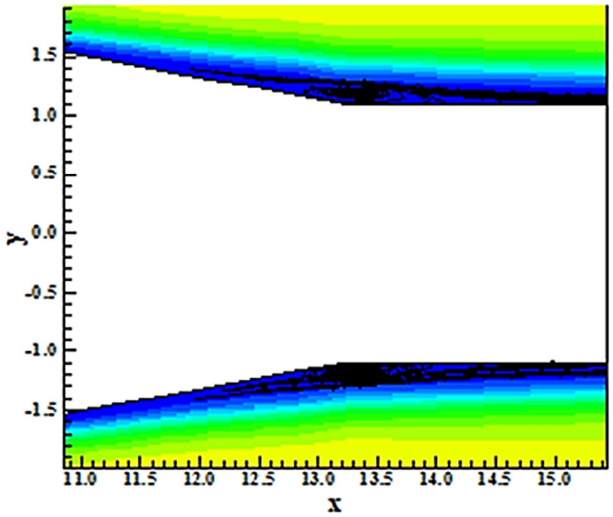

Figure 58. *Circulation bubble formation (Cockpit-GA-CC).*

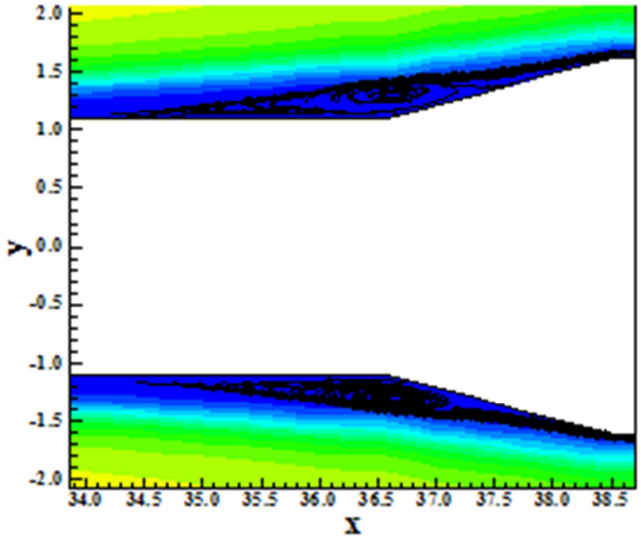

Figure 59. *Circulation bubble formation (Boosters-GA-CC).*

Figure 60 shows the –Cp distribution obtained with the [20] turbulence model. The step profile at the blunt nose region and the hole region at the booster region are again observable. The pressure recovery at the booster region is typical of all solutions in this study. This –Cp profile is not so strength than the [17] and [18] profiles and is similar to the [19] profiles.

As main conclusion of this four turbulence models studied herein, the [17] model is the less dissipative in qualitative terms. However, the [19] turbulence model gives more severe temperature fields than the others. Moreover, the [17] and [18] turbulence models predict more intense –Cp distributions.

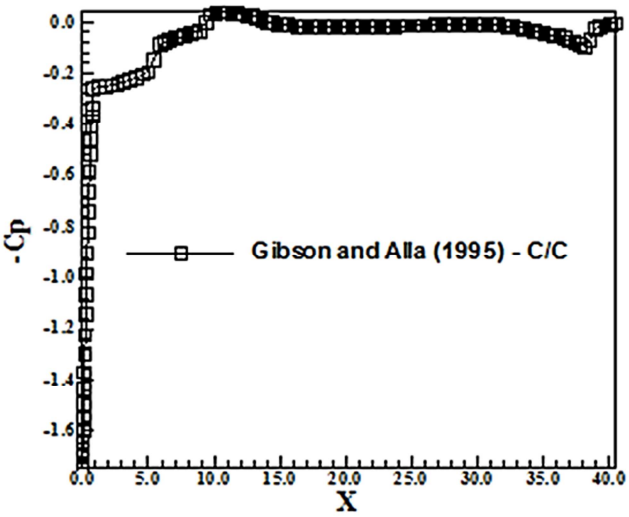

Figure 60. *–Cp distribution (GA-CC).*

5.5. Quantitative Analysis

Table 3 shows the lift and drag aerodynamic coefficients calculated by the [2] scheme in the turbulent cases. As the geometry is symmetrical and an attack angle of zero value was adopted in the simulations, the lift coefficient should have a zero value. The most correct value to the lift coefficient is due to the [20] turbulence model, in its C-LS variant.

Table 3. *Aerodynamic coefficients of lift and drag.*

Turbulence Model:	c_L:	c_D:
[17] turbulence model	-6.261×10^{-5}	0.072
[18] turbulence model	5.412×10^{-6}	0.072
[19] turbulence model - Wilcox	-4.978×10^{-6}	0.074
[19] turbulence model – TL	2.431×10^{-6}	0.074
[19] turbulence model – BSL	1.009×10^{-6}	0.074
[19] turbulence model – SST	-7.785×10^{-6}	0.074
[20] turbulence model – LS-LS	-8.230×10^{-6}	0.072
[20] turbulence model – LS-C	-4.531×10^{-6}	0.072
[20] turbulence model – C-LS	9.960×10^{-8}	0.072
[20] turbulence model – C-C	-5.392×10^{-6}	0.072

Another possibility to quantitative comparison of the laminar and turbulent cases is the determination of the stagnation pressure ahead of the configuration. [27] presents a table of normal shock wave properties in its B Appendix. This table permits the determination of some shock wave properties as function of the freestream Mach number. In front of the VLS configuration, the shock wave presents a normal shock behavior, which permits the determination of the stagnation pressure, behind the shock wave, from the tables encountered in [27]. So it is possible to determine the ratio pr_0/pr_∞ from [27], where pr_0 is the stagnation pressure in front of the configuration and pr_∞ is the freestream pressure (equals to $1/\gamma$ to the present dimensionless).

Hence, to this problem, $M_\infty = 3.0$ corresponds to $pr_0/pr_\infty =$

12.06 and remembering that $pr_\infty = 0.714$, it is possible to conclude that $pr_0 = 8.61$. Values of the stagnation pressure to the turbulent cases and respective percentage errors are shown in Tab. 4. They are obtained from Figures 3, 9, 13, 19, 25, 31, 37, 43, 49, and 55. As can be observed, the [19] turbulence model, in all four variants, present the best result, with a percentage error of 4.70%.

Table 4. *Values of the stagnation pressure and respective percentage errors.*

Turbulence Model:	pr_0:	Error (%):
[17] turbulence model	7.90	8.10
[18] turbulence model	8.10	5.80
[19] turbulence model - Wilcox	8.20	4.70
[19] turbulence model – TL	8.20	4.70
[19] turbulence model – BSL	8.20	4.70
[19] turbulence model – SST	8.20	4.70
[20] turbulence model – LS-LS	8.00	7.00
[20] turbulence model – LS-C	8.00	7.00
[20] turbulence model – C-LS	8.00	7.00
[20] turbulence model – C-C	8.00	7.00

Finally, Table 5 exhibits the computational data of the present simulations. It can be noted that the most efficient is the [19] turbulence model in its SST variant.

Table 5. *Computational data.*

Turbulence Model:	CFL:	Iterations:
[17] turbulence model	0.10	5,100
[18] turbulence model	0.05	12,829
[19] turbulence model – Wilcox	0.10	4,315
[19] turbulence model – TL	0.10	4,657
[19] turbulence model – BSL	0.10	4,328
[19] turbulence model – SST	0.10	4,289
[20] turbulence model – LS-LS	0.10	6,075
[20] turbulence model – LS-C	0.10	6,115
[20] turbulence model – C-LS	0.10	6,035
[20] turbulence model – C-C	0.10	6,062

As final conclusion of this study, the [20] turbulence model in its BSL variant was the best when comparing these four turbulence models: [17-20]. This choice is based on the second best estimative of the aerodynamic coefficients and the best estimative to the stagnation pressure.

6. Conclusion

In the present work, the [2] flux vector splitting scheme is implemented, on a finite-volume context. The two-dimensional Favre-averaged Navier-Stokes equations are solved using an upwind discretization on a structured mesh. The [17] one-equation model and the [18-20] two-equation models are used in order to close the problem. The physical problem under study is the supersonic flow around a simplified version of the VLS configuration. The implemented scheme uses a MUSCL procedure to reach second order accuracy in space. The time integration uses a Runge-Kutta method of five stages and is second order accurate. The algorithm is accelerated to the steady state solution using a spatially variable time step. This technique has proved excellent gains as reported in [21-22].

The results have demonstrated that the [19] model has yielded more critical temperature fields than the other models. The aerodynamic coefficient of lift is better predicted by the [20] turbulence model in its Chien-Launder and Sharma variant, with the [19] in its BSL variant in second place. The stagnation pressure ahead of the VLS configuration is better predicted by the [19] turbulence model in its BSL variant. Hence, the best choice corresponds to the [19] turbulence model in its BSL variant for this study.

In a next paper, the present author will study more four different turbulent models to this same problem trying to identify the best of each group of four and to perform a final analysis to found the best one.

Acknowledgment

The author would like to thank the infrastructure of ITA that allowed the realization of this work.

References

[1] P. Kutler, “Computation of Three-Dimensional, Inviscid Supersonic Flows”, *Lecture Notes in Physics*, vol. 41, pp. 287-374, 1975.

[2] B. Van Leer, “Flux-Vector Splitting for the Euler Equations”, Proceedings of the 8th International Conference on Numerical Methods in Fluid Dynamics, E. Krause, Editor, *Lecture Notes in Physics*, vol. 170, pp. 507-512, Springer-Verlag, Berlin, 1982.

[3] R. Radespiel, and N. Kroll, “Accurate Flux Vector Splitting for Shocks and Shear Layers”, *Journal of Computational Physics*, vol. 121, pp. 66-78, 1995.

[4] E. S. G. Maciel, “Assessment of Several Turbulence Models as Applied to Supersonic Flows in 2D – Part I”, Submitted to *Engineering and Technology* (under review), 2015.

[5] E. S. G. Maciel, and N. G. C. R. Fico Jr., “Estudos de Escoamentos Turbulentos Utilizando o Modelo de Baldwin e Lomax e Comparação entre Algoritmos Explícitos e Implícitos”, *Proceedings of the III National Congress of Mechanical Engineering (III CONEM)*, Belém, PA, Brazil, 2004. [CD-ROM]

[6] B. S. Baldwin, and H. Lomax, “Thin Layer Approximation and Algebraic Model for Separated Turbulent Flows”, *AIAA Paper 78-257*, 1978.

[7] R. W. MacCormack, “The Effect of Viscosity in Hypervelocity Impact Cratering”, *AIAA Paper 69-354*, 1969.

[8] T. H. Pulliam, and D. S. Chaussee, “A Diagonal Form of an Implicit Approximate-Factorization Algorithm”, *Journal of Computational Physics*, vol. 39, pp. 347-363, 1981.

[9] A. Jameson, W. Schmidt, and E. Turkel, "Numerical Solution of the Euler Equations by Finite Volume Methods Using Runge-Kutta Time Stepping Schemes", *AIAA Paper 81-1259*, 1981.

[10] E. S. G. Maciel, and N. G. C. R. Fico Jr., "High Resolution Algorithms Coupled with Three Turbulence Models Applied to an Aerospace Flow Problem – Part I", *AIAA Paper 06-0292*, 2006. [CD-ROM]

[11] T. Cebeci, and A. M. O. Smith, "A Finite-Difference Method for Calculating Compressible Laminar and Turbulent Boundary Layers", *Journal of Basic Engineering,* Trans. ASME, Series B, vol. 92, no. 3, pp. 523-535, 1970.

[12] P. R. Sparlat, and S. R. Allmaras, "A One-Equation Turbulence Model for Aerodynamic Flows", *AIAA Paper 92-0439*, 1992.

[13] A. Harten, "High Resolution Schemes for Hyperbolic Conservation Laws", *Journal of Computational Physics*, vol. 49, pp. 357-393, 1983.

[14] E. S. G. Maciel, and N. G. C. R. Fico Jr., "Comparação Entre Modelos de Turbulência de Duas Equações Aplicados a um Problema Aeroespacial", *Proceedings of the Primer Congreso Argentino de Ingeniería Mecánica (I CAIM),* Bahía Blanca, Argentina, 2008. [CD-ROM]

[15] F. Jacon, and D. Knight, "A Navier-Stokes Algorithm for Turbulent Flows Using an Unstructured Grid and Flux Difference Splitting", *AIAA Paper 94-2292*, 1994.

[16] Y. Kergaravat, and D. Knight, "A Fully Implicit Navier-Stokes Algorithm for Unstructured Grids Incorporating a Two-Equation Turbulence Model", *AIAA Paper 96-0414*, 1996.

[17] P. R. Sparlat, and S. R. Allmaras, "A One-Equation Turbulence Model for Aerodynamic Flows", *AIAA Paper 92-0439*, 1992.

[18] F. Jacon, and D. Knight, "A Navier-Stokes Algorithm for Turbulent Flows Using an Unstructured Grid and Flux Difference Splitting", *AIAA Paper 94-2292*, 1994.

[19] F. R. Menter, and C. L. Rumsey, "Assessment of Two-Equation Turbulence Models for Transonic Flows", *AIAA Paper 94-2343*, 1994.

[20] M. M. Gibson, and A. A. Dafa'Alla, "Two-Equation Model for Turbulent Wall Flow", *AIAA Journal*, Vol. 33, No. 8, pp. 1514-1518, 1995.

[21] E. S. G. Maciel, "Analysis of Convergence Acceleration Techniques Used in Unstructured Algorithms in the Solution of Aeronautical Problems – Part I", *Proceedings of the XVIII International Congress of Mechanical Engineering (XVIII COBEM)*, Ouro Preto, MG, Brazil, 2005. [CD-ROM]

[22] E. S. G. Maciel, "Analysis of Convergence Acceleration Techniques Used in Unstructured Algorithms in the Solution of Aerospace Problems – Part II", *Proceedings of the XII Brazilian Congress of Thermal Engineering and Sciences (XII ENCIT)*, Belo Horizonte, MG, Brazil, 2008. [CD-ROM]

[23] R. W. Fox, and A. T. McDonald, "*Introdução à Mecânica dos Fluidos*", Ed. Guanabara Koogan, Rio de Janeiro, RJ, Brazil, 632 p, 1988.

[24] E. S. G. Maciel, "Comparação entre os Modelos de Turbulência de Cebeci e Smith e de Baldwin e Lomax", *Proceedings of the 5th Spring School of Transition and Turbulence (V EPTT)*, Rio de Janeiro, RJ, Brazil, 2006. [CD-ROM]

[25] E. S. G. Maciel, "Estudo de Escoamentos Turbulentos Utilizando os Modelos de Cebeci e Smith e de Baldwin e Lomax e Comparação entre os Algoritmos de MacCormack e de Jameson e Mavriplis", *Proceedings of the 7th Symposium of Computational Mechanics (VII SIMMEC),* Araxá, MG, Brazil, 2006. [CD-ROM]

[26] E. S. G. Maciel, "Assessment of Several Turbulence Models as Applied to Supersonic Flows in 2D – Part II", Submitted to *Engineering and Technology* (under review), 2015.

[27] J. D. Anderson Jr., "*Fundamentals of Aerodynamics*", McGraw-Hill, Inc., EUA, 563p, 1984.

[28] F. R. Menter, "Zonal Two Equation k-ω Turbulence Models for Aerodynamic Flows", *AIAA Paper 93-2906*, 1993.

[29] D. C. Wilcox, "Reassessment of the Scale-Determining Equation for Advanced Turbulence Models", *AIAA Journal*, Vol. 26, No. 11, pp. 1299-1310, 1988.

[30] B. E. Launder, and B. I. Sharma, Application of the Energy-Dissipation Model of Turbulence to the Calculation of Flow Near a Spinning Disc, *Letters in Heat and Mass Transfer*, Vol. 1, No. 2, pp. 131-138, 1974.

[31] K. Y. Chien, "Predictions of Channel and Boundary Layer Flows with a Low-Reynolds-Number Turbulence Model", *AIAA Journal*, Vol. 20, January, pp. 33-38, 1982.